

Perfectly Matched Layers versus discrete transparent boundary conditions in quantum device simulations

Jan-Frederik Mennemann ^{*} Ansgar Jüngel [†]

December 6, 2013

Abstract

Discrete transparent boundary conditions (DTBC) and the Perfectly Matched Layers (PML) method for the realization of open boundary conditions in quantum device simulations are compared, based on the stationary and time-dependent Schrödinger equation. The comparison includes scattering state, wave packet, and transient scattering state simulations in one and two space dimensions. The Schrödinger equation is discretized by a second-order Crank-Nicolson method in case of DTBC. For the discretization with PML, symmetric second-, fourth, and sixth-order spatial approximations as well as Crank-Nicolson and classical Runge-Kutta time-integration methods are employed. In two space dimensions, a ring-shaped quantum waveguide device is simulated in the stationary and transient regime. As an application, a simulation of the Aharonov-Bohm effect in this device is performed, showing the excitation of bound states localized in the ring region. The numerical experiments show that the results obtained from PML are comparable to those obtained using DTBC, while keeping the high numerical efficiency and flexibility as well as the ease of implementation of the former method.

Keywords: Schrödinger equation, Perfectly Matched Layers, discrete transparent boundary conditions, transient simulations, quantum waveguides, Aharonov-Bohm effect

1 Introduction

The electron transport in nanoscale electronic devices, in which inelastic collisional effects may be neglected, can be modeled by the stationary or time-dependent Schrödinger equation. The semiconductor device is typically connected to semi-infinite leads which describe

^{*}jfmennemann@gmx.de, Institute for Analysis and Scientific Computing, Vienna University of Technology, Wiedner Hauptstraße 8–10, 1040 Vienna, Austria

[†]juengel@tuwien.ac.at, Institute for Analysis and Scientific Computing, Vienna University of Technology, Wiedner Hauptstraße 8–10, 1040 Vienna, Austria

the electric contacts. The aim is to solve the Schrödinger problem in the bounded device domain instead in the whole space. This makes it necessary to prescribe appropriate open boundary conditions at the interface between the leads and the active region of the device to avoid unphysical reflections at the boundary. In the literature, several methods have been proposed to derive transparent boundary conditions. Analytical transparent boundary conditions are nonlocal in time, and their numerical implementation requires some care (see the review [2] and references therein). Moreover, inadequate discretizations may introduce strong reflections at the boundary.

In this paper, we implement and compare two approaches: the discrete transparent boundary conditions (DTBC), which are completely reflection-free at the boundary but nonlocal in time, and the Perfectly Matched Layers (PML), which involve an artificial boundary layer but which can be implemented very efficiently.

In the context of finite-difference discretizations, DTBC were derived by Arnold [4]. They yield unconditionally stable reflection-free numerical discretizations. DTBC include the discrete convolution of the unknown function with a given kernel, whose numerical computation is rather involved. The evaluation can be significantly accelerated by approximating the kernel by a finite sum of exponentials which decay with respect to time [6]. The limit of vanishing spatial approximation parameters in the DTBC coincides with the temporally semi-discrete transparent boundary conditions of [22, 19]. DTBC for the Schrödinger equation were also derived for finite-element [30] and splitting higher-order schemes [14].

The PML approach was introduced by Bérenger [8] for absorbing boundaries for wave equations. The idea is to replace the absorbing boundary condition by an absorbing boundary layer which damps out waves using a damping function. The problem of having reflections from the absorber boundary was handled by Bérenger by constructing a special absorbing medium. PML can be seen as the result of a complex coordinate transformation, being essentially a continuation of the Schrödinger equation into complex spatial coordinates [11]. Later, PML were derived and analyzed for many other equations, like wave and Helmholtz equations [26] and Schrödinger equations [12]. Nonlinear Schrödinger problems were investigated in, for instance, [10, 28, 29]. The simulations include (stationary) scattering state calculations [10] or wave packets [28, 29]. However, transient scattering states which are needed to describe the time-dependent behavior of quantum devices are not considered.

In a transient scattering state simulation, the initial wave function is given by a (stationary) scattering state. When the transient simulation is started, the external potential is allowed to change over time and hence, the scattering state starts to evolve in time too.

Our aim is to provide a careful numerical comparison between DTBC and PML in the finite-difference context. We show how PML can be applied in a variety of physical situations: (stationary) scattering states, wave packets, incoming waves, and transient scattering states. In the following, we describe our approach and the main results in more detail.

Since the open boundary problem for quantum waveguides in several space dimensions can be reduced to the one-dimensional case, we consider one-dimensional simulations first.

The Schrödinger equation is discretized using symmetric finite differences of second, fourth, and sixth order. The numerical solutions obtained from (second-order) DTBC and (second- and higher-order) PML are compared in a series of simulations. It turns out that for second-order discretizations, PML compete well with DTBC for medium to large energies ($10 \dots 1000$ meV). For very small energies ($10^{-3} \dots 1$ meV), second-order DTBC perform significantly better than second-order PML, but the numerical errors for higher-order PML schemes are comparable to that for second-order DTBC at small energies and they are much smaller for medium to large energies.

Then we turn to two-dimensional quantum waveguide simulations. The stationary scattering state problem has been solved in [18] using linear finite elements along with exact transparent boundary conditions. The transient case is considered in [7, 23] using DTBC based on the Crank-Nicolson scheme. However, transient scattering states are not considered and the cross sections of the leads need to be infinite square well potentials. In this paper, we show how to remove these limitations. Although we consider only ring-shaped two-terminal quantum waveguides, our approach can also be applied to more complicated multi-terminal devices.

The implementation of open boundary conditions using PML works analogously to the one-dimensional case. Contrary to DTBC, a decomposition into cross-sectional waveguide eigenstates is not required, which simplifies the implementation significantly. Our simulations indicate that the numerical error which results from the PML is of the same order as that resulting from the approximation of the Schrödinger equation itself. In contrast to DTBC, which are tailored specifically to numerical methods, PML can be applied in a more flexible way. As an example, we employ second-, fourth-, and sixth-order finite-difference formulas to approximate the spatial derivatives. For the time integration, we use the Crank-Nicolson approximation and classical Runge-Kutta methods.

The Runge-Kutta approach has the drawback that the resulting spatio-temporal discretization is only conditionally stable and that the mass of the particles is not conserved exactly. Our numerical results suggest, however, that these issues may be overestimated. The advantages are the competitive computing times, the high accuracy for higher-order schemes, and the easy implementation. The combination of the classical Runge-Kutta method, higher-order spatial discretizations, and PML appears to be a very efficient approach for transient quantum device simulations.

Finally, we apply the above mentioned methods in a simulation of the Aharonov-Bohm effect [1]. Transient simulations of the Aharonov-Bohm effect were also studied in the literature. For instance, the electron transport in a quantum ring, using an expansion of the wave function in a basis of Gaussians and a finite-difference approach, was considered in [25]. Simulations of ring-quantum interference transistors, where the Aharonov-Bohm effect is studied in dependence of externally applied electrostatic potentials, are shown in [16]. However, these works do not include transient scattering state simulations. As far as we know, we present in this paper the first two-dimensional transient scattering state simulations of the Aharonov-Bohm effect in a ring-shaped quantum waveguide. Remarkably, we find that fast variations of the external magnetic field lead to the excitation of bound states which are localized in the ring region.

The paper is organized as follows. Section 2 covers stationary scattering states, wave packets, and transient scattering states in one space dimension. We recall the discretization of the Schrödinger equation using DTBC, detail the approximation employing PML, and compare both methods numerically. In Section 3, we consider two-dimensional ring-shaped quantum waveguide devices. The derivation of DTBC and PML for the stationary and transient problems is detailed. Section 4 is devoted to the Aharonov-Bohm effect in the stationary and transient regime.

2 One-dimensional simulations

2.1 Scattering states

Scattering states in one-dimensional simulations represent a beam of electrons injected at the left or right lead of the device. This beam of particles is identified with a wave function which solves the stationary Schrödinger equation

$$-\frac{\hbar^2}{2m^*} \frac{d^2}{dx^2} \phi(x) + V(x)\phi(x) = E\phi(x), \quad x \in \mathbb{R}, \quad (1)$$

subject to the boundary condition at infinity that the incoming wave function is a plane wave. Here, E denotes the total energy, V the potential energy, \hbar the reduced Planck constant, and m^* the effective mass of the electrons in the semiconductor. In all subsequent simulations, we choose $m^* = 0.067 m_e$, corresponding to the effective mass of electrons in GaAs, with m_e being the electron mass at rest.

The device in $(0, L)$ is assumed to be connected to the semi-infinite leads $(-\infty, 0]$ and $[L, \infty)$. In the exterior domain $(-\infty, 0] \cup [L, \infty)$, the potential energy is assumed to be constant, i.e. $V(x) = V_\ell$ for $x \leq 0$ and $V(x) = V_r$ for $x \geq L$. Without loss of generality we set $V_\ell = 0$ and $V_r = -eU$, where e denotes the elementary charge and U is the applied voltage at the right contact.

The energy of an electron injected at the left contact is given by $E(k) = \hbar^2 k^2 / (2m^*)$, where $k > 0$ denotes the electron wave number in the left lead. The incoming electron is represented by a plane wave $\exp(ikx)$ traveling to the right. Accordingly, transparent boundary conditions read as [5]

$$\phi'(0) + ik\phi(0) = 2ik, \quad \phi'(L) = i\sqrt{2m^*(E - V_r)/\hbar^2} \phi(L). \quad (2)$$

Electrons injected at the right contact traveling to the left are treated analogously.

Discrete transparent boundary conditions. A symmetric second-order finite-difference discretization of the stationary Schrödinger equation (1) on the equidistant grid $x_j = j\Delta x$, $j \in \mathbb{Z}$, with $x_J = L$ and $\Delta x > 0$ is given by

$$-\frac{\hbar^2}{2m^*} \frac{\phi_{j-1} - 2\phi_j + \phi_{j+1}}{(\Delta x)^2} + V_j \phi_j = E\phi_j. \quad (3)$$

As before, the potential energy in the semi-infinite leads is assumed to be constant, i.e., $V_j = 0$ for $j \leq 0$ and $V_j = -eU$ for $j \geq J$. We seek for a solution of (3) restricted to the grid

$$X_{\text{DTBC}} = \{x_j = j\Delta x, j = 0, \dots, J\}, \quad (4)$$

and hence we have to specify boundary conditions at $x_0 = 0$ and $x_J = L$. It is well known that a direct discretization of the transparent boundary conditions in (2) via standard finite-difference formulas may lead to spurious oscillations in the numerical solution. These oscillations may be eliminated using DTBC [5]. The idea is to derive the boundary conditions on the discrete level of equation (3). In the semi-infinite leads, the potential energy is assumed to be constant and thus, (3) admits two solutions of the form $\phi_j = \alpha_{\ell,r}^j$, where the numbers

$$\alpha_{\ell,r} = 1 - \frac{m^* E_{\ell,r}^{\text{kin}}(k)(\Delta x)^2}{\hbar^2} \pm i \sqrt{\frac{2m^* E_{\ell,r}^{\text{kin}}(k)(\Delta x)^2}{\hbar^2} - \frac{(m^*)^2 E_{\ell,r}^{\text{kin}}(k)^2 (\Delta x)^4}{\hbar^4}}$$

depend on the kinetic energy $E_{\ell,r}^{\text{kin}}(k) = E(k) - V_{\ell,r}$ in the left or right lead, respectively.

Depending on $|\alpha_{\ell,r}| \leq 1$, the solutions are exponentially decreasing or increasing. In case $|\alpha_{\ell,r}| = 1$ the solutions are discrete plane waves (see below) unless $\alpha_{\ell,r} = 1$ in which case they are constant. For a wave function injected at the left contact traveling to the right, the solution to (3) is a superposition of an incoming and a reflected discrete plane wave, $\phi_j = A\alpha_{\ell}^j + B\alpha_{\ell}^{-j}$ in the left contact, and a transmitted wave $\phi_j = C\alpha_r^j$ in the right contact. The amplitude of the incoming discrete plane wave in the left lead is set to $A = 1$. Eliminating B and C yields the desired DTBC

$$\phi_0 - \alpha_{\ell}\phi_1 = 1 - \alpha_{\ell}^2, \quad \alpha_r\phi_{J-1} - \phi_J = 0. \quad (5)$$

Here, we implicitly assumed $V_j = 0$ for $j \leq 1$ and $V_j = -eU$ for $j \geq J - 1$ but we could just as easily state the boundary conditions in terms of ϕ_{-1}, ϕ_0 and ϕ_J, ϕ_{J+1} .

On the discrete level of equation (3), we need to replace the continuous E - k -relation

$$k = \sqrt{2m^* E^{\text{kin}}}/\hbar \quad (6)$$

by the discrete E - k -relation

$$k = \arccos(1 - m^*(\Delta x/\hbar)^2 E^{\text{kin}})/\Delta x, \quad (7)$$

which approximates the continuous relation up to second order. Consequently, the discrete solutions can be written as $\phi_j = \exp(\pm ikj\Delta x)$ and hence for $|\alpha_{0,J}^{\pm}| = 1$, they are called discrete plane waves. Plane waves injected at the right contact traveling to the left are treated analogously. For further details we refer to [5].

Perfectly Matched Layers. PML can be formulated using the complex coordinate transformation

$$x \mapsto x + e^{i\pi/4} \int^x \sigma(x') dx', \quad (8)$$

with the absorption function

$$\sigma(x) = \begin{cases} \sigma_0(x_\ell^* - x)^p & \text{for } x < x_\ell^*, \\ 0 & \text{for } x_\ell^* \leq x \leq x_r^*, \\ \sigma_0(x - x_r^*)^p & \text{for } x_r^* < x. \end{cases}$$

This coordinate transformation corresponds to the substitution

$$\frac{d}{dx} \rightarrow c(x) \frac{d}{dx}, \quad c(x) := \frac{1}{1 + e^{i\pi/4}\sigma(x)}, \quad (9)$$

such that the stationary Schrödinger-PML equation reads as

$$-\frac{\hbar^2}{2m^*} c(x) \frac{d}{dx} \left(c(x) \frac{d}{dx} \phi(x) \right) + V(x) \phi(x) = E \phi(x), \quad x \in \mathbb{R}. \quad (10)$$

This agrees with the original stationary Schrödinger equation (1) for $x \in [x_\ell^*, x_r^*]$, and hence we require that $[0, L] \subset [x_\ell^*, x_r^*]$. Outside of $[x_\ell^*, x_r^*]$, propagating waves are damped exponentially fast,

$$\exp(ikx) \rightarrow \exp(ikx) \exp \left(ike^{i\pi/4} \int^x \sigma(x') dx' \right), \quad (11)$$

with their distance to the points $x_{\ell,r}^*$. Denoting the thickness of the PML by d_0 , the computational domain is given by $[x_\ell^* - d_0, x_r^* + d_0]$. We use cubic absorption functions ($p = 3$), which we found to give slightly better results than the quadratic functions used in [28].

A wave propagating through a PML is expected to be practically zero when it hits the boundary of the computational domain, provided d_0 is sufficiently large. Therefore, either Dirichlet or Neumann boundary conditions can be imposed at the boundary points $x_\ell^* - d_0$ and $x_r^* + d_0$. We discuss this issue below in more detail.

Propagating waves with different wave numbers k experience different attenuation according to (11). A uniform attenuation independent of the wave number can be obtained by including $1/k$ in the absorption function. This strategy is typically used in stationary wave problems [24]. Since we are concerned mainly with transient simulations, we employ a different strategy.

Any wave packet can be thought of as a superposition of propagating waves of different energy or different wave number k . For that reason, we seek for PML which are able to treat all incoming waves simultaneously. In this spirit, the factor $\exp(i\pi/4)$ appearing in (8) is meant to give a good effect on average as explained in [28]. The thickness of the PML will be comparatively large as they are not optimized to absorb waves of a single energy. In the simulations below, we fix the thickness of the PML first. Then we choose the absorption strength factor σ_0 such that the numerical error becomes sufficiently small for a given range of energies.

We use symmetric finite-difference formulas to approximate the modified spatial derivative $c(x)\partial_x(c(x)\partial_x) = c(x)c'(x)\partial_x + c(x)^2\partial_x^2$ in (10). Approximations of second, fourth and sixth order read as

$$\tilde{D}_x^{2,2\text{nd}}\phi_j := c(x_j)c'(x_j)D_x^{1,2\text{nd}}\phi_j + c^2(x_j)D_x^{2,2\text{nd}}\phi_j, \quad (12a)$$

$$\tilde{D}_x^{2,4\text{th}}\phi_j := c(x_j)c'(x_j)D_x^{1,4\text{th}}\phi_j + c^2(x_j)D_x^{2,4\text{th}}\phi_j, \quad (12b)$$

$$\tilde{D}_x^{2,6\text{th}}\phi_j := c(x_j)c'(x_j)D_x^{1,6\text{th}}\phi_j + c^2(x_j)D_x^{2,6\text{th}}\phi_j, \quad (12c)$$

where the abbreviations

$$D_x^{1,2\text{nd}}\phi_j := (-\phi_{j-1} + \phi_{j+1})/(2\Delta x), \quad (13a)$$

$$D_x^{1,4\text{th}}\phi_j := (\phi_{j-2} - 8\phi_{j-1} + 8\phi_{j+1} - \phi_{j+2})/(12\Delta x), \quad (13b)$$

$$D_x^{1,6\text{th}}\phi_j := (-\phi_{j-3} + 9\phi_{j-2} - 45\phi_{j-1} + 45\phi_{j+1} - 9\phi_{j+2} + \phi_{j+3})/(60\Delta x), \quad (13c)$$

$$D_x^{2,2\text{nd}}\phi_j := (\phi_{j-1} - 2\phi_j + \phi_{j+1})/(\Delta x)^2, \quad (13d)$$

$$D_x^{2,4\text{th}}\phi_j := (-\phi_{j-2} + 16\phi_{j-1} - 30\phi_j + 16\phi_{j+1} - \phi_{j+2})/(12(\Delta x)^2), \quad (13e)$$

$$D_x^{2,6\text{th}}\phi_j := (2\phi_{j-3} - 27\phi_{j-2} + 270\phi_{j-1} - 490\phi_j + 270\phi_{j+1} - 27\phi_{j+2} + 2\phi_{j+3}^{(n)})/(180(\Delta x)^2), \quad (13f)$$

are needed frequently in the following. We further introduce the equidistant grid

$$X_{\text{PML}} := \{x_j = x_\ell^* - d_0 + j\Delta x, j = 0, \dots, J_{\text{PML}}\} \quad (14)$$

with $x_{J_{\text{PML}}} = x_r^* + d_0$ and $X_{\text{DTBC}} \subset X_{\text{PML}}$. Then the discrete stationary Schrödinger-PML equation reads

$$-\frac{\hbar^2}{2m^*}\tilde{D}_x^2\phi_j + V_j\phi_j = E\phi_j, \quad \tilde{D}_x^2 \in \{\tilde{D}_x^{2,2\text{nd}}, \tilde{D}_x^{2,4\text{th}}, \tilde{D}_x^{2,6\text{th}}\}. \quad (15)$$

At the boundaries of X_{PML} , we impose homogeneous Dirichlet or Neumann boundary conditions. In the latter case, \tilde{D}_x^2 is modified accordingly.

We still need to specify how to realize an incoming plane wave at, say, the left contact. To simplify the presentation, we restrict ourselves to the second-order discretization $\tilde{D}_x^2 = \tilde{D}_x^{2,2\text{nd}}$. Let $x_{j_0} = 0$ denote the boundary of the left contact. The wave function in the left contact is given by the sum of an incoming and a reflected wave function $\phi_j = \phi_j^{\text{inc}} + \phi_j^{\text{refl}}$. In the numerical implementation, we eliminate ϕ_j^{inc} in the left lead. Thus, to realize an incoming plane wave at x_{j_0} , the finite difference equations for $j_0 - 1$ and j_0 need to be modified according to

$$-\frac{\hbar^2}{2m^*}\frac{\phi_{j_0-2} - 2\phi_{j_0-1} + (\phi_{j_0} - \phi_{j_0}^{\text{inc}})}{(\Delta x)^2} + V_{j_0-1}\phi_{j_0-1} = E\phi_{j_0-1}, \quad (16a)$$

$$-\frac{\hbar^2}{2m^*}\frac{(\phi_{j_0-1} + \phi_{j_0-1}^{\text{inc}}) - 2\phi_{j_0} + \phi_{j_0+1}}{(\Delta x)^2} + V_{j_0}\phi_{j_0} = E\phi_{j_0}. \quad (16b)$$

We note that the absorption function of the left lead is only active for $x_j \leq x_\ell^*$. Choosing x_ℓ^* slightly smaller than x_{j_0} ensures that the complex function c does not show up in (16). Therefore, the final numerical problem becomes

$$-\frac{\hbar^2}{2m^*} \tilde{D}_x^{2,2\text{nd}} \phi_j + (V_j - E) \phi_j = b_j, \quad j = 0, \dots, J_{\text{PML}},$$

where

$$b_j = \begin{cases} -(\hbar^2/(2m^*(\Delta x)^2)) \phi_{j_0}^{\text{inc}} & \text{for } j = j_0 - 1, \\ +(\hbar^2/(2m^*(\Delta x)^2)) \phi_{j_0-1}^{\text{inc}} & \text{for } j = j_0, \\ 0 & \text{else.} \end{cases}$$

For higher-order approximations $\tilde{D}_x^2 = \tilde{D}_x^{2,4\text{th}}$ or $\tilde{D}_x^2 = \tilde{D}_x^{2,6\text{th}}$, we proceed in a similar way. However, due to the extended finite-difference stencils, the vector b involves four or six non-zero entries, respectively.

The incoming plane wave is given by $\phi_j^{\text{inc}} = \exp(ikj\Delta x)$. In case of the second-order discretization, the wave number is related to the kinetic energy by the discrete E - k -relation (7). In case of the higher-order discretizations, we simply use (6), since the corresponding discrete k - E -relations cannot easily be inverted and the differences would be small anyhow.

Simulations. We consider the ramp-like potential energy

$$V(x) = \begin{cases} 0 & \text{for } x < a_0, \\ -\frac{x - a_0}{a_1 - a_0} eU & \text{for } a_0 \leq x < a_1, \\ -eU & \text{for } x \geq a_1, \end{cases} \quad (17)$$

with $a_0 = 40$ nm, $a_1 = 80$ nm, and $U = -25$ mV. The device extends from 0 nm to $L = 120$ nm. The electrons are injected at the left contact traveling to the right. At the left contact, the potential energy is zero, and hence the energy of the incoming electrons is given by the kinetic energy only, which is denoted by $E_{\text{kin}}^{\text{inc}}$. We choose the width $d_0 = 40$ nm of the PML, the absorption strength factor $\sigma_0 = 0.02$, and the mesh size $\Delta x = 0.5$ nm. Unless stated otherwise, the simulations in this subsection are performed using homogeneous Neumann boundary conditions at the end points of the PML.

Figure 1 shows the real parts of scattering states computed with DTBC (dotted line) and PML (solid line) for different energies $E_{\text{kin}}^{\text{inc}}$. The distances of x_ℓ^* and x_r^* to the device domain are a few times the mesh size Δx , which ensures that the discretization inside the device domain is not altered by the PML. We note that the second-order discretizations with DTBC and PML coincide exactly inside the device domain. Indeed, Figure 1 shows that the scattering states of both methods, computed for different values of $E_{\text{kin}}^{\text{inc}}$, can hardly be distinguished.

Figure 1 (top) corresponds to the energy $E_{\text{kin}}^{\text{inc}} = 15$ meV. Since the potential energy at the right contact amounts to 25 meV, all incoming electrons are being reflected and then absorbed by the PML in the left contact. The discontinuity in the wave function at

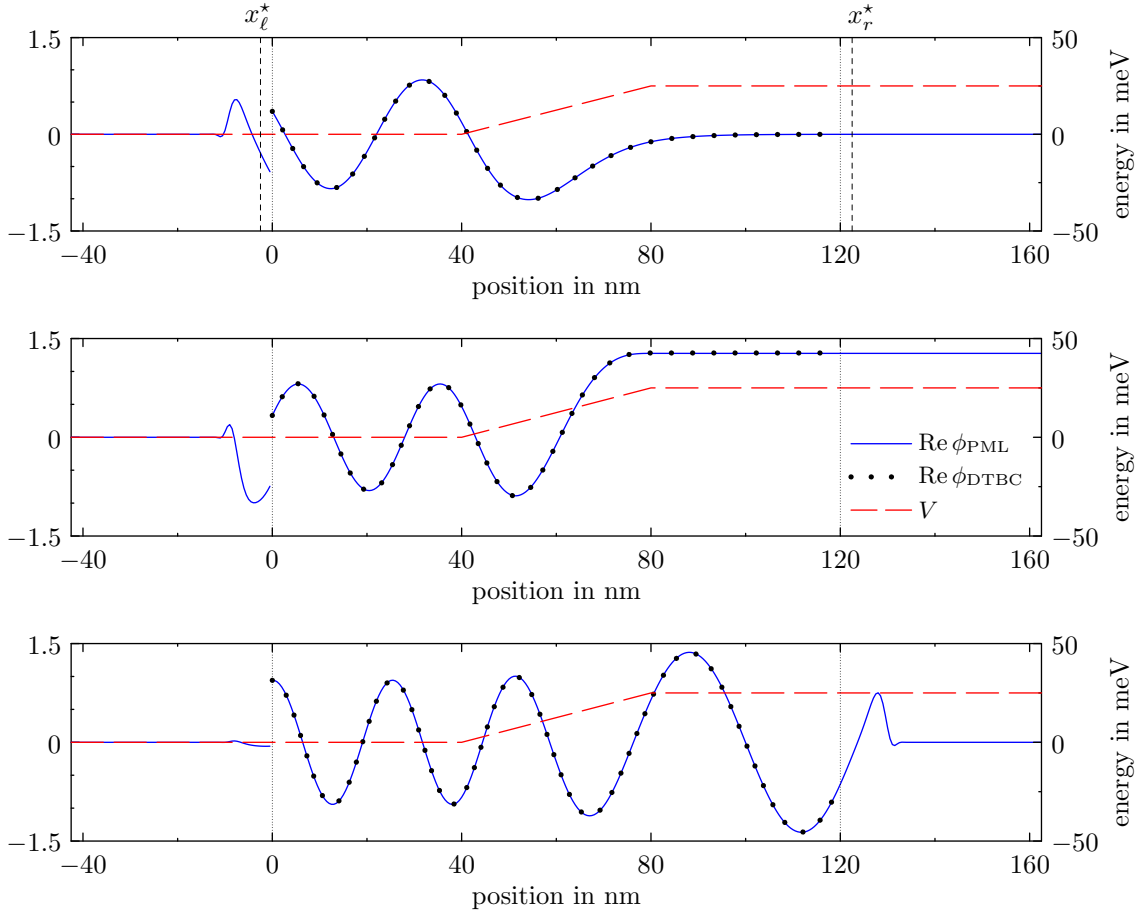


Figure 1: Scattering states for an electron injected at the left contact. The kinetic energy of the incoming electrons is $E_{\text{inc}}^{\text{kin}} = 15$ meV (top), 25 meV (center), and 35 meV (bottom). The points x_{ℓ}^* and x_r^* indicate the boundaries of the PML in the left and right lead, respectively.

$x = 0$ nm stems from the fact that the incoming plane wave in the left contact has been eliminated.

The middle figure corresponds to the limiting case $E_{\text{kin}}^{\text{inc}} = 25$ meV, i.e., electrons which reach the contact on the right-hand side have zero kinetic energy. Hence, the wave number becomes zero and according to (11), the PML in the right contact has no effect on the wave function. Nonetheless, we obtain a reasonable approximation due to the Neumann boundary conditions imposed at the boundary of the computational domain. However, the question arises whether the PML fails when $E_{\text{inc}}^{\text{kin}}$ is very close to this critical energy. This issue will be addressed below.

Figure 1 (bottom) corresponds to $E_{\text{kin}}^{\text{inc}} = 35$ meV. Since the potential energy of the transmitted electrons is increased by 25 meV, the kinetic energy is decreased by this amount which results in a reduced wave number, or equivalently, in an increased wavelength.

We repeat the same numerical experiment, but this time we compute scattering states for the whole range of energies $E_{\text{kin}}^{\text{inc}} \in [10^{-3}, 10^3]$ meV. Simultaneously, we calculate (quasi)-

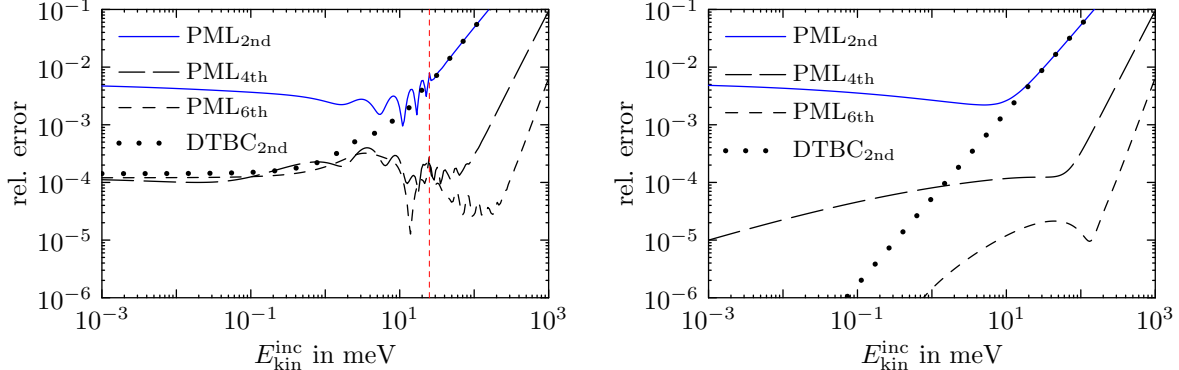


Figure 2: Relative errors of the scattering states as a function of the kinetic energy with applied voltage $U = -25$ mV (left) and $U = 0$ (right). The critical energy $E_{\text{kin}}^{\text{inc}} = 25$ meV is marked by the dashed vertical line.

exact reference solutions. This is possible since the potential energy is a piecewise linear function [20, 27]. The relative errors in the ℓ^2 -norm for different numerical methods are depicted in Figure 2 (left). It turns out that $\text{DTBC}_{2\text{nd}}$ and $\text{PML}_{2\text{nd}}$ yield similar results for medium to large energies. For very small energies, $\text{DTBC}_{2\text{nd}}$ performs significantly better than $\text{PML}_{2\text{nd}}$. Moreover, the higher-order methods $\text{PML}_{4\text{th}}$ and $\text{PML}_{6\text{th}}$ yield much smaller errors than $\text{DTBC}_{2\text{nd}}$ for energies $E_{\text{kin}}^{\text{inc}} \gtrsim 1$ meV. We remark that a smaller mesh size Δx yields similar curves which are shifted downwards.

For zero potential energy $V = 0$, the scattering state solutions to the stationary Schrödinger equation are simple plane waves. The relative errors, to which we will return later, are shown in Figure 2 (right).

Next, we compute scattering states for the ramp-like potential energy and $E_{\text{kin}}^{\text{inc}} \in [24.9999, 25.0001]$ meV, i.e., for energies extremely close to the critical energy $E_{\text{kin}}^{\text{inc}} = 25$ meV. This time, we use Dirichlet or Neumann boundary conditions at the end points of the PML and employ two different mesh sizes $\Delta x = 0.5$ nm and $\Delta x = 0.1$ nm. The numerical errors corresponding to Dirichlet boundary conditions are depicted in the left column of Figure 3 and those corresponding to Neumann boundary conditions are shown in the right column.

For $\Delta x = 0.5$ nm (top row), we observe only a small perturbation of the numerical errors around the critical value. In case of $\text{PML}_{2\text{nd}}$, the effect is obscured completely by the error of the spatial discretization, which is present even if transparent boundary conditions are used (compare $\text{DTBC}_{2\text{nd}}$). For $\Delta x = 0.1$ nm (bottom row), the effect becomes more pronounced since the spatial discretization error is greatly reduced. However, the maximum error is essentially the same. This holds also true for smaller Δx and finer sampling of $E_{\text{kin}}^{\text{inc}}$. For $E_{\text{kin}}^{\text{inc}} = 25$ meV the Neumann boundary condition is exact and hence, the numerical error is minimized.

For that reason we prefer Neumann boundary conditions at the end points of the computational domain in all subsequent simulations. Apart from this, both boundary

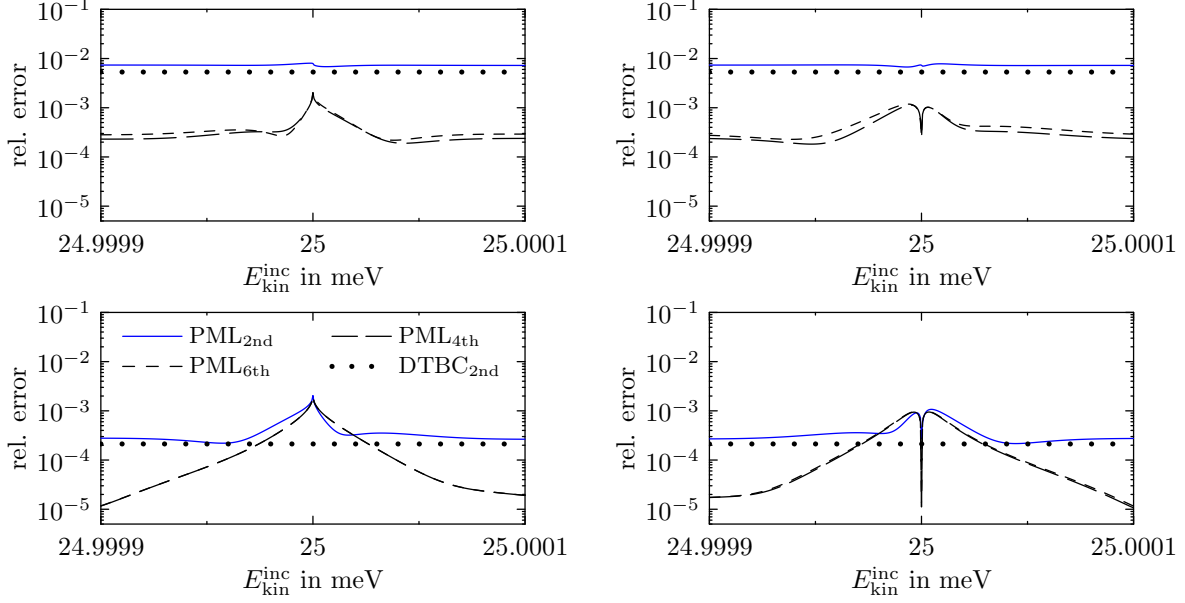


Figure 3: Close-up view of the relative errors of the scattering states as a function of the kinetic energy using Dirichlet (left column) or Neumann boundary conditions (right column) at the end points of the PML with mesh sizes $\Delta x = 0.5$ nm (top row) and $\Delta x = 0.1$ nm (bottom row).

conditions provide essentially the same results. In summary, we found that the accuracy of the numerical methods using PML is reduced if the wave number of an incident wave function approaches zero. However, in practice this effect is comparatively small.

2.2 Wave packets

We consider the one-dimensional time-dependent Schrödinger equation,

$$i\hbar \frac{\partial}{\partial t} \psi(x, t) = -\frac{\hbar^2}{2m^*} \frac{\partial^2}{\partial x^2} \psi(x, t) + V(x, t)\psi, \quad \psi(\cdot, 0) = \psi_0, \quad x \in \mathbb{R}, t > 0. \quad (18)$$

Under the assumptions that the initial wave function is compactly supported in $(0, L)$ and that the potential in the exterior domain vanishes, $V(x, t) = 0$ for $x \leq 0$ and $x \geq L$, $t \geq 0$, it is well known [5] that transparent boundary conditions at $x = 0$ and $x = L$ read as

$$\frac{\partial \psi}{\partial x}(x, t)|_{x=0,L} = \pm \sqrt{\frac{2m^*}{\pi\hbar}} e^{-i\pi/4} \frac{d}{dt} \int_0^t \frac{\psi(x, \tau)|_{x=0,L}}{\sqrt{t-\tau}} d\tau. \quad (19)$$

Using (19) one can easily derive transparent boundary conditions for non-zero exterior potentials which are spatially constant but may change with time [3]. As an example, we consider $V(x, t) = V_r(t)$ for $x \geq L$, $t \geq 0$ and $V_r(t) = -eU(t)$, where $U(t)$ is the applied

voltage. To get rid of the potential in the right lead, we define the gauge change

$$\tilde{\psi}(x, t) := \exp\left(\frac{i}{\hbar} \int_0^t V_r(s) ds\right) \psi(x, t) \quad x \geq L, t \geq 0.$$

This function solves the free Schrödinger equation and consequently, (19) yields a transparent boundary condition for a time-dependent exterior potential in the right lead:

$$\frac{\partial \psi}{\partial x}(x, t)|_{x=L} = -\sqrt{\frac{2m^*}{\pi\hbar}} e^{-i\pi/4} e^{-i \int_0^t V_r(s) ds/\hbar} \frac{d}{dt} \int_0^t \frac{e^{i \int_0^\tau V_r(s) ds/\hbar} \psi(x, \tau)|_{x=L}}{\sqrt{t-\tau}} d\tau.$$

Discrete transparent boundary conditions. The three-point finite-difference discretization (13d) applied to the time-dependent Schrödinger equation (18) yields the semi-discretized problem

$$\frac{d}{dt} \psi_j(t) = i \frac{\hbar}{2m^*} D_x^{2,2\text{nd}} \psi_j(t) - \frac{i}{\hbar} V(t) \psi_j(t) =: f(t, \psi_j(t)), \quad (20)$$

which is solved by the Crank-Nicolson time-integration method

$$\psi^{(n+1)} = \psi^{(n)} + \Delta t f((n+1/2)\Delta t, \psi^{(n+1/2)}). \quad (21)$$

Replacing $\psi_j^{(n+1/2)}$ by the average value $(\psi_j^{(n+1)} + \psi_j^{(n)})/2$ yields the well-known Crank-Nicolson scheme

$$\left(I - \frac{i\hbar\Delta t}{4m^*} D_x^2 + \frac{i\Delta t}{2\hbar} V_j^{(n+1/2)}\right) \psi_j^{(n+1)} = \left(I + \frac{i\hbar\Delta t}{4m^*} D_x^2 - \frac{i\Delta t}{2\hbar} V_j^{(n+1/2)}\right) \psi_j^{(n)} \quad (22)$$

on the equidistant grid $x_j = j\Delta x$, $t_n = n\Delta t$ with $j \in \mathbb{Z}$ and $n \in \mathbb{N}_0$. For zero exterior potentials, the corresponding DTBC at the left ($x_0 = 0$) and the right ($x_J = L$) contact are given as follows [4]:

$$\psi_1^{(n+1)} - s^{(0)} \psi_0^{(n+1)} = \sum_{\ell=1}^n s^{(n+1-\ell)} \psi_0^{(\ell)} - \psi_1^{(n)}, \quad n \geq 0, \quad (23a)$$

$$\psi_{J-1}^{(n+1)} - s^{(0)} \psi_J^{(n+1)} = \sum_{\ell=1}^n s^{(n+1-\ell)} \psi_J^{(\ell)} - \psi_{J-1}^{(n)}, \quad n \geq 0, \quad (23b)$$

with the convolution coefficients

$$s^{(n)} = \left(1 - i\frac{R}{2}\right) \delta_{n,0} + \left(1 + i\frac{R}{2}\right) \delta_{n,1} + \alpha e^{-in\varphi} \frac{P_n(\mu) - P_{n-2}(\mu)}{2n-1}$$

and the abbreviations

$$R = \frac{4m(\Delta x)^2}{\hbar\Delta t}, \quad \varphi = \arctan \frac{4}{R}, \quad \mu = \frac{R}{\sqrt{R^2 + 16}}, \quad \alpha = \frac{i}{2} \sqrt{R^2(R^2 + 16)} e^{i\varphi/2}.$$

Here, P_n denotes the n th-degree Legendre polynomial ($P_{-1} = P_{-2} = 0$), and $\delta_{n,j}$ is the Kronecker symbol. The Crank-Nicolson scheme (22) with the DTBC (23) yields an unconditionally stable discretization which is perfectly free of reflections [4, 5]. The corresponding solution coincides exactly with the solution of the discrete whole space problem (22) restricted to the grid X_{DTBC} defined in (4). Time-dependent exterior potentials may be included like in the continuous case described above (see [21] for details).

Perfectly Matched Layers. We apply the coordinate transformation (8) also in the transient case, which yields the time-dependent Schrödinger-PML equation

$$i\hbar \frac{\partial}{\partial t} \psi(x, t) = -\frac{\hbar^2}{2m^*} c(x) \frac{\partial}{\partial x} \left(c(x) \frac{\partial}{\partial x} \psi(x, t) \right) + V(x, t) \psi(x, t), \quad (24)$$

where $c(x)$ is defined in (9). Accordingly, the semi-discretized problem is given by (20), wherein $D_x^{2,\text{2nd}}$ is replaced by $\tilde{D}_x^2 \in \{\tilde{D}_x^{2,\text{2nd}}, \tilde{D}_x^{2,\text{4th}}, \tilde{D}_x^{2,\text{6th}}\}$ (see (12)). The spatial grid X_{PML} is the same as in the stationary case (see (14)). Using the Crank-Nicolson time-integration method gives (22) but with the modified spatial differential operator \tilde{D}_x^2 .

Alternatively, we solve this problem via the classical (explicit) Runge Kutta method. In quantum mechanics simulations, this method is used very rarely. This is probably because the resulting spatio-temporal discretization is only conditionally stable. Moreover, the norm of the wave function is not a conserved quantity, i.e., in general $\|\psi^{(n+1)}\|_{\ell^2}^2 = \|\psi^{(n)}\|_{\ell^2}^2$ does not hold exactly. We address these issues in a simple numerical experiment where we solve the ordinary time-dependent Schrödinger equation (without PML) for a harmonic oscillator potential $V(x) = m^* \omega_* x^2 / 2$ with $\omega_* = 0.25 \times 10^{14} \text{ s}^{-1}$. As a reference solution, we consider a so called coherent state [15],

$$\psi(x, t) = \left(\frac{m^* \omega_*}{\pi \hbar} \right)^{1/4} \exp \left(-\frac{m^* \omega_*}{2\hbar} \left(x^2 - 2xx_0 e^{-i\omega_* t} + \frac{x_0^2}{2} e^{-2i\omega_* t} + \frac{x_0^2}{2} \right) - \frac{i}{2} \omega_* t \right),$$

where $x_0 = 10 \text{ nm}$ denotes the expectation value of the particle at $t = 0$. The computational domain extends from -50 nm to 50 nm . Near the boundaries, the wave function is zero (to numerical precision) and hence it is reasonable to employ homogeneous Dirichlet boundary conditions. The initial state $\psi(x, 0)$ is propagated for 100 000 time steps using the Runge-Kutta scheme. The spatial derivative is approximated by $D_x^{2,\text{2nd}}$, $D_x^{2,\text{4th}}$, or $D_x^{2,\text{6th}}$. Using $\Delta x = 0.5 \text{ nm}$ and $\Delta t = 0.1 \text{ fs}$, we obtain the deviation from the initial mass, $|\|\psi^{(100\,000)}\|_{\ell^2} / \|\psi^{(0)}\|_{\ell^2} - 1| \lesssim 5.9 \times 10^{-11}$, independent of the spatial discretization. Moreover, the relative errors of the final wave functions are given by 2.19×10^{-1} , 6.56×10^{-4} , and 6.42×10^{-6} corresponding to $D_x^{2,\text{2nd}}$, $D_x^{2,\text{4th}}$, and $D_x^{2,\text{6th}}$, respectively. In the recent paper [9], the stability bounds $\Delta t < \kappa (\Delta x)^2$ for the linear and nonlinear Schrödinger equation were derived for second- and fourth-order spatial discretizations. Remarkably, the constants κ stated in [9] agree with our experimental findings, even if we solve the Schrödinger-PML equation. In case of the sixth-order spatial discretization, our numerical experiments suggest that κ needs to be adapted slightly by a factor 3/4 compared to κ in the fourth-order discretization. In fact, $\kappa = 9m^*/(8\sqrt{2}N\hbar)$, where N denotes the space dimension, gives almost sharp bounds for the simulations presented in this paper.

Simulations. We solve the time-dependent Schrödinger equation (18) for zero potential energy. As a reference solution, we choose a superposition of three Gaussian wave packets,

$$\xi_p(x, t) = \left(1 + i\frac{t}{\tau}\right)^{-1/2} \exp \left[\left(1 + i\frac{t}{\tau}\right)^{-1} \left(-\left(\frac{x - x_0}{2\sigma}\right)^2 + ik_p(x - x_0) - i\sigma^2 k_p^2 \frac{t}{\tau} \right) \right], \quad (25)$$

where $\tau = 2m^*\sigma^2/\hbar$ and $k_p = \sqrt{2m^*E_p}/\hbar$, $p = 1, 2, 3$. At $t = 0$, each Gaussian is centered around $x_0 = L/2$. Using $\sigma = 7.5$ nm, the initial wave packet is practically zero outside the device domain $[0, L] = [0, 120]$ nm. The average energy of the first, second, and third Gaussian is $E_1 = 0$ meV, $E_2 = 25$ meV, and $E_3 = 75$ meV, respectively. Therefore, the reference solution is a superposition of propagating plane waves $\exp(ikx - i\omega t)$ of very low to high energies $E = (\hbar k)^2/(2m^*)$ with the wave frequency $\omega = E/\hbar$. We use the same spatial mesh size $\Delta x = 0.5$ nm and the same parameters of the PML as for the scattering state simulations. The time step size is given by $\Delta t = 0.1$ fs.

Figure 4 shows the relative ℓ_2 errors of simulations using DTBC or PML. At the beginning of the simulation, the two second-order methods yield similar results. During this phase, the numerical error is dominated by the fast traveling parts of the wave packet, since their oscillations in space and time are difficult to handle by low order methods. Shortly afterwards, the relative error of the PML solution is stabilizing around the value 3×10^{-3} . This agrees with the numerical errors presented in Figure 2 (right) since at later times, the wave packet can be thought of as a superposition of primarily low energy plane wave scattering states. In contrast, the numerical error of the DTBC solution decreases continuously.

Figure 4 also shows the numerical errors according to higher-order methods. For example, a sixth-order spatial discretization in combination with PML reduces the maximum relative error by more than two orders of magnitude. The maximum error can be reduced further by replacing the second-order Crank-Nicolson time-integration method with the fourth-order Runge-Kutta method. In this case, even the fast temporal oscillations in the beginning of the simulation are resolved with high accuracy.

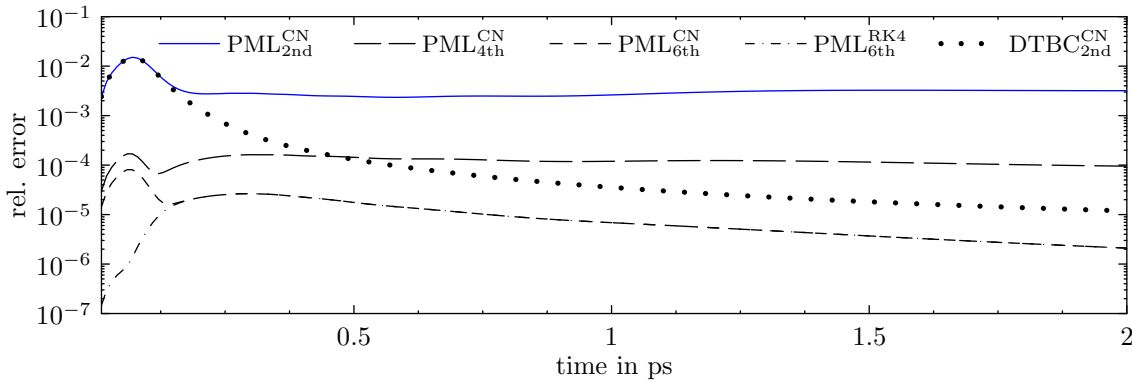


Figure 4: Relative errors versus time for different numerical methods corresponding to the simulation using three Gaussian wave packets.

2.3 Time-dependent incoming waves

Before we turn our attention to transient scattering state simulations, we explain how to realize an incoming wave at a device boundary. As an example, we consider the free time-dependent Schrödinger equation, where an incident plane wave

$$\psi^{\text{inc}}(x, t) = \exp(ikx - i\omega t), \quad x \leq 0, \quad \omega = \hbar k^2 / (2m^*),$$

is prescribed at $x = 0$ nm. The transparent boundary condition at $x = L$ is as in (19). However, at $x = 0$ we need to prescribe an inhomogenous transparent boundary condition which follows if we apply (19) to the wave $\psi - \psi^{\text{inc}}$ [3, 5]:

$$\frac{\partial}{\partial x} (\psi(x, t) - \psi^{\text{inc}}(x, t)) \Big|_{x=0} = \sqrt{\frac{2m^*}{\pi\hbar}} e^{-i\pi/4} \frac{d}{dt} \int_0^t \frac{\psi(0, \tau) - \psi^{\text{inc}}(0, \tau)}{\sqrt{t - \tau}} d\tau. \quad (26)$$

To avoid a discontinuity at $(x, t) = (0, 0)$, we assume compatibility of the initial and boundary data at this point (see [5] for details).

Discrete transparent boundary conditions. The discrete analogue of (26) for the Crank-Nicolson scheme (22) follows by replacing $\psi_j^{(n)}$ by $\psi_j^{(n)} - \phi_j^{(n)}$ in (23a),

$$\psi_1^{(n+1)} - s^{(0)}\psi_0^{(n+1)} = \sum_{\ell=1}^n s^{(n+1-\ell)} \left(\psi_0^{(\ell)} - \phi_0^{(\ell)} \right) - \left(\psi_1^{(n)} - \phi_1^{(n)} \right) + \phi_1^{(n+1)} - s^{(0)}\phi_0^{(n+1)}.$$

Here,

$$\phi_j^{(n)} = \exp(ikx_j - i\omega n\Delta t) \quad (27)$$

represents an incoming discrete plane wave, i.e., k is related to $E = E_{\text{kin}}^{\text{inc}}$ according to the discrete E - k -relation (7), and the wave frequency is given by the discrete E - ω -relation

$$\omega = \frac{2}{\Delta t} \arctan \left(\frac{E\Delta t}{2\hbar} \right), \quad (28)$$

which is the discrete analogue of $\omega = E/\hbar$ (see [5]).

Perfectly Matched Layers. We solve the transient Schrödinger-PML equation (24), where an incoming time-dependent plane wave is prescribed at one of the device boundaries. The incoming wave is realized analogously to the case of the stationary scattering state simulations. As an example, we consider the Crank-Nicolson scheme (22) with D_x^2 replaced by $\tilde{D}_x^2 = \tilde{D}_x^{2, \text{2nd}}$. In the vicinity of the device boundary $x_{j_0} = 0$, the potential energy is zero, but more importantly, the PML is inactive. The wave function in the left contact is a superposition of an incoming and a reflected wave. However, the incoming wave (27) is eliminated in the left lead and hence $\psi_j^{(n)}$ represents the reflected wave for $j < j_0$.

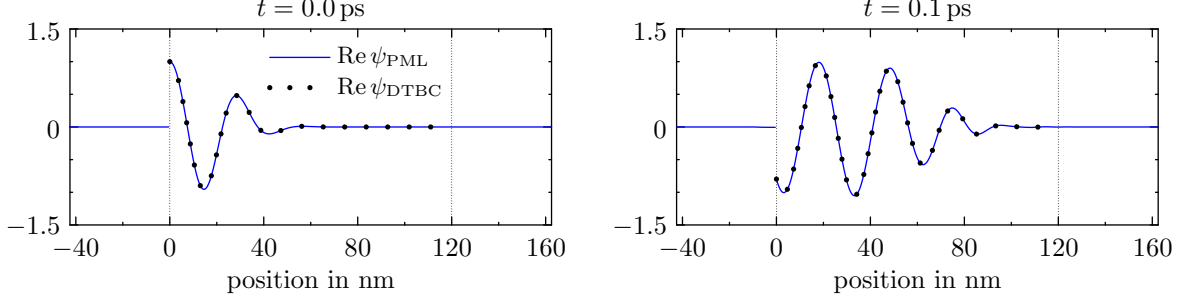


Figure 5: An incoming plane wave with energy $E_{\text{kin}}^{\text{inc}} = 25$ meV at the left contact using PML (solid line) and DTBC (dotted line).

Accordingly, the finite-difference equations for $j_0 - 1$ and j_0 need to be modified as follows:

$$\begin{aligned}
\psi_{j_0-1}^{(n+1)} - \frac{i\hbar\Delta t}{4m^*(\Delta x)^2} \left[\psi_{j_0-2}^{(n+1)} - 2\psi_{j_0-1}^{(n+1)} + (\psi_{j_0}^{(n+1)} - \phi_{j_0}^{(n+1)}) \right] \\
= \psi_{j_0-1}^{(n)} + \frac{i\hbar\Delta t}{4m^*(\Delta x)^2} \left[\psi_{j_0-2}^{(n)} - 2\psi_{j_0-1}^{(n)} + (\psi_{j_0}^{(n)} - \phi_{j_0}^{(n)}) \right], \\
\psi_{j_0}^{(n+1)} - \frac{i\hbar\Delta t}{4m^*(\Delta x)^2} \left[(\psi_{j_0-1}^{(n+1)} + \phi_{j_0-1}^{(n+1)}) - 2\psi_{j_0}^{(n+1)} + \psi_{j_0+1}^{(n+1)} \right] \\
= \psi_{j_0}^{(n)} + \frac{i\hbar\Delta t}{4m^*(\Delta x)^2} \left[(\psi_{j_0-1}^{(n)} + \phi_{j_0-1}^{(n)}) - 2\psi_{j_0}^{(n)} + \psi_{j_0+1}^{(n)} \right].
\end{aligned} \tag{29}$$

Since $\phi_{j_0}^{(n)}$ and $\phi_{j_0-1}^{(n)}$ are known for all $n \in \mathbb{N}_0$, we collect these values,

$$b_j^{(n)} = \begin{cases} -\frac{i\hbar\Delta t}{4m^*(\Delta x)^2} (\phi_{j_0}^{(n+1)} + \phi_{j_0}^{(n)}) & \text{for } j = j_0 - 1, \\ +\frac{i\hbar\Delta t}{4m^*(\Delta x)^2} (\phi_{j_0-1}^{(n+1)} + \phi_{j_0-1}^{(n)}) & \text{for } j = j_0, \\ 0 & \text{else} \end{cases}$$

on the right-hand side of (22). In case $\tilde{D}_x^2 = \tilde{D}_x^{2,4\text{th}}$ and $\tilde{D}_x^2 = \tilde{D}_x^{2,6\text{th}}$, we proceed in a similar way. However, due to the extended finite-difference stencils, four or six finite-difference equations need to be modified accordingly. If the semi-discretized problem is solved via the Runge-Kutta method, the incoming wave needs to be taken into account at each of the four intermediate Runge-Kutta time-steps.

Simulations. An incoming plane wave is depicted in Figure 5 at $t = 0$ ps and $t = 0.1$ ps. The potential energy is zero everywhere and the kinetic energy of the incoming electrons amounts to $E_{\text{kin}}^{\text{inc}} = 25$ meV. We note that it would take quite a long time (compared to the underlying time scale) before the wave function becomes approximately stationary.

2.4 Transient scattering states

A transient scattering state simulation describes a quantum device in which a continuously incoming plane wave is prescribed at one of the device contacts. Moreover, the potential energy is allowed to change with time. The lead potentials need to be spatially constant but may depend on time too. In contrast to the simulation depicted in Figure 5, one is typically not interested in the initial transient phase. Instead of waiting for the wave function to become stationary for the first time, it is preferable to initialize the simulation with a scattering state. This situation is considered in [5] where the potential energy is switched instantaneously. An extension to continuously time-variable potentials can be found in [21].

As an example, we consider the time-dependent Schrödinger equation with the ramp-like potential (17), where the applied voltage U is assumed to be time-dependent with $U(t) = U_0$ for $t \leq 0$. The initial wave function is given by the scattering state solution ϕ of the stationary Schrödinger equation for the potential energy according to U_0 . As before, we consider electrons injected at the left contact with energy $E = E_{\text{kin}}^{\text{inc}}$. For the sake of completeness, we state the corresponding boundary conditions [5, 21]:

$$\begin{aligned} \frac{\partial}{\partial x} [\psi(x, t) - e^{-iEt/\hbar} \phi(x)] \Big|_{x=0} \\ = + \sqrt{\frac{2m^*}{\pi\hbar}} e^{-i\pi/4} \frac{d}{dt} \int_0^t \frac{\psi(0, \tau) - e^{-iE\tau/\hbar} \phi(0)}{\sqrt{t-\tau}} d\tau, \end{aligned} \quad (30a)$$

$$\begin{aligned} \frac{\partial}{\partial x} \left[e^{i \int_0^t V_r(s) ds/\hbar} \psi(x, t) - e^{-i(E-V_r(0))t/\hbar} \phi(x) \right] \Big|_{x=L} \\ = - \sqrt{\frac{2m^*}{\pi\hbar}} e^{-i\pi/4} \frac{d}{dt} \int_0^t \frac{e^{i \int_0^\tau V_r(s) ds/\hbar} \psi(L, \tau) - e^{-i(E-V_r(0))\tau/\hbar} \phi(L)}{\sqrt{t-\tau}} d\tau. \end{aligned} \quad (30b)$$

Here, $V_r(t) = -eU(t)$ denotes the potential energy in the right lead.

Discrete transparent boundary conditions. The discrete analogue of (30a) follows by replacing $\psi_j^{(n)}$ by $\psi_j^{(n)} - \beta^{(n)} \phi_j$ in (23a),

$$\begin{aligned} (\psi_1^{(n+1)} - \beta^{(n+1)} \phi_1) - s^{(0)} (\psi_0^{(n+1)} - \beta^{(n+1)} \phi_0) \\ = \sum_{\ell=1}^n s^{(n+1-\ell)} (\psi_0^{(\ell)} - \beta^{(\ell)} \phi_0) - (\psi_1^{(n)} - \beta^{(n)} \phi_1), \end{aligned} \quad (31)$$

where ϕ_j is a solution of the discrete scattering state problem outlined above. The discretization of the gauge-change term,

$$\beta^{(n)} = \exp(-2in \arctan(\Delta t E / (2\hbar))) \approx \exp(-iEt/\hbar),$$

is consistent with the underlying Crank-Nicolson time-integration method [21]. Similarly,

the discrete analogue of (30b) follows by replacing $\psi_j^{(n)}$ by $\epsilon^{(n)}\psi_j^{(n)} - \gamma^{(n)}\phi_j$ in (23b):

$$\begin{aligned} & (\epsilon^{(n+1)}\psi_{J-1}^{(n+1)} - \gamma^{(n+1)}\phi_{J-1}) - s^{(0)}(\epsilon^{(n+1)}\psi_J^{(n+1)} - \gamma^{(n+1)}\phi_J) \\ &= \sum_{\ell=1}^n s^{(n+1-\ell)}(\epsilon^{(\ell)}\psi_J^{(\ell)} - \gamma^{(\ell)}\phi_J) - (\epsilon^{(n)}\psi_{J-1}^{(n)} - \gamma^{(n)}\phi_{J-1}). \end{aligned} \quad (32)$$

The gauge-change terms are approximated via

$$\begin{aligned} \gamma^{(n)} &= \exp(2in(\arctan(\Delta t V_r^{(0)}/(2\hbar)) - \arctan(\Delta t E/(2\hbar))) \\ &\approx \exp(-i(E - V_r(0))t/\hbar), \\ \epsilon^{(n)} &= \exp\left(\frac{i}{\hbar} \sum_{\ell=0}^{n-1} \arctan(\Delta t V_r^{(\ell+1/2)})\right) \approx \exp\left(\frac{i}{\hbar} \int_0^t V_r(s) ds\right), \end{aligned} \quad (33)$$

which is also compatible with the underlying Crank-Nicolson method. We note that the Crank-Nicolson scheme along with the inhomogeneous DTBC (31) and (32) is still perfectly free of spurious reflections. In fact, (31) and (32) yield an exact truncation of the discrete whole-space problem.

Perfectly Matched Layers. No further steps are necessary to realize a transient scattering state simulation using PML. Given the potential energy at $t = 0$ and the kinetic energy $E_{\text{kin}}^{\text{inc}}$ of the electrons injected at the device contact, we compute a scattering state solution of the discrete stationary Schödinger-PML equation. This scattering state serves as the initial state of the transient problem where a time-dependent incoming plane wave (27) is prescribed at the device contact.

Simulations. Figure 6 shows the time evolution of a transient scattering state. The incoming plane wave at the left contact represents electrons with a kinetic energy of $E_{\text{kin}}^{\text{inc}} = 25$ meV traveling to the right. The applied voltage $U(t)$ is illustrated in Figure 7 (top left). Accordingly, we initialize the simulation with the scattering state corresponding to an applied voltage of $U_0 = -100$ mV. Until $t = 0.5$ ps we keep the applied voltage constant and hence the numerical solution remains the same. More precisely, $|\psi|^2$ remains the same while $\text{Re } \psi$ oscillates with time.

From $t = 0.5$ ps up to $t = 12.5$ ps, the applied voltage varies corresponding to a medium oscillation with a large amplitude and a fast oscillation with a smaller amplitude. As a result, the wave function shows a wild behavior as indicated in the second, third, and fourth row of Figure 6. For times $t \geq 12.5$ ps, the voltage is kept constant at $U = 0$ mV. The last row of Figure 6 shows that even at $t = 20$ ps, the wave function has not become perfectly stationary again. The time evolution of the scattering state is available as a movie at <http://www.asc.tuwien.ac.at/~juengel>.

The simulation described above was carried out using the second-order Crank-Nicolson scheme with DTBC or PML with the time step size of $\Delta t = 0.1$ fs. Inside the device domain both discretizations coincide exactly. Since DTBC represent an exact truncation of the discrete whole-space problem, the relative difference of both methods results from

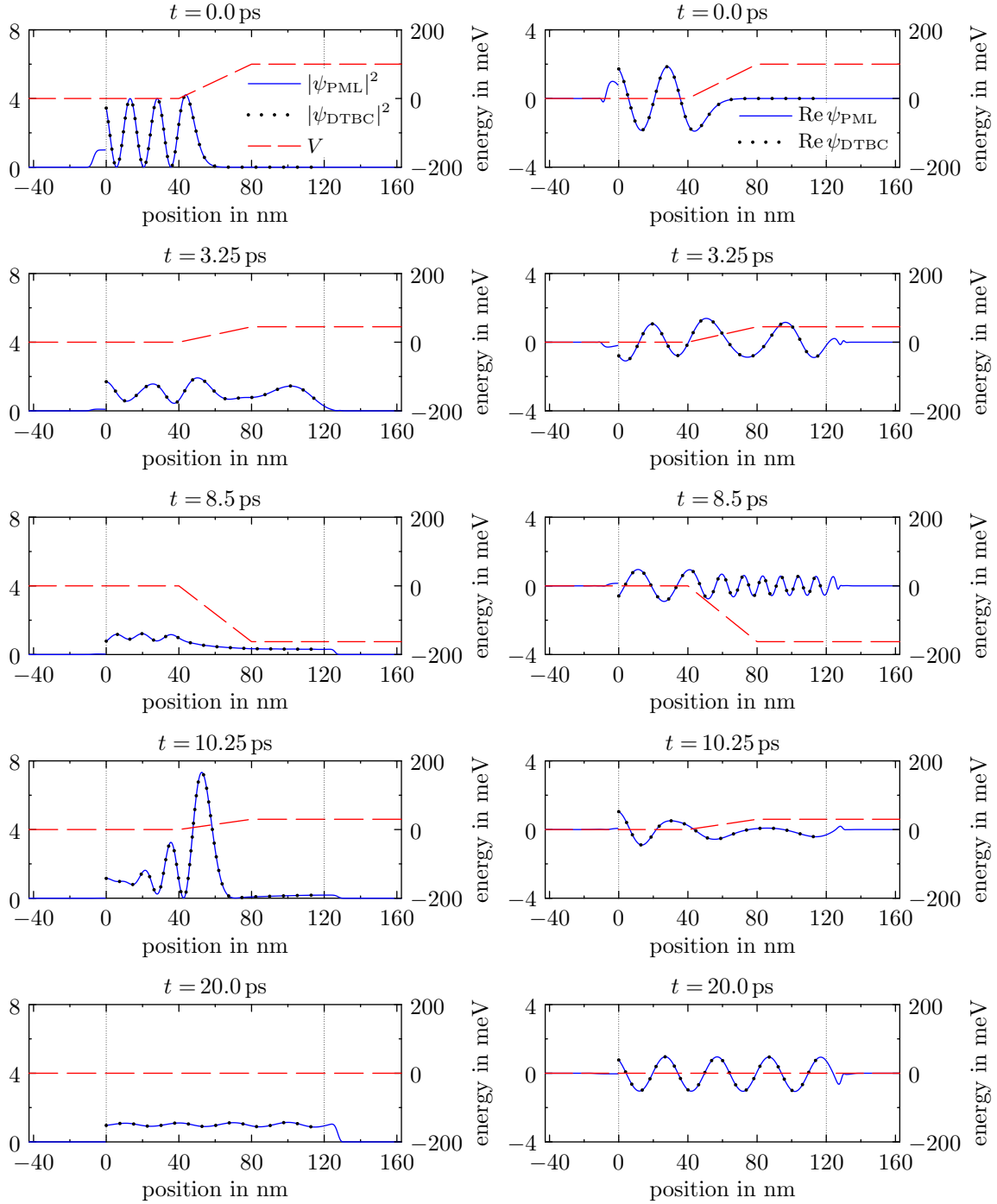


Figure 6: Transient scattering state $|\psi|^2$ (left column) and $\text{Re } \psi$ (right column) at selected times for a continuously incoming plane wave prescribed at the left contact. The incoming plane wave corresponds to electrons with a kinetic energy of $E_{\text{kin}}^{\text{inc}} = 25$ meV traveling to the right.

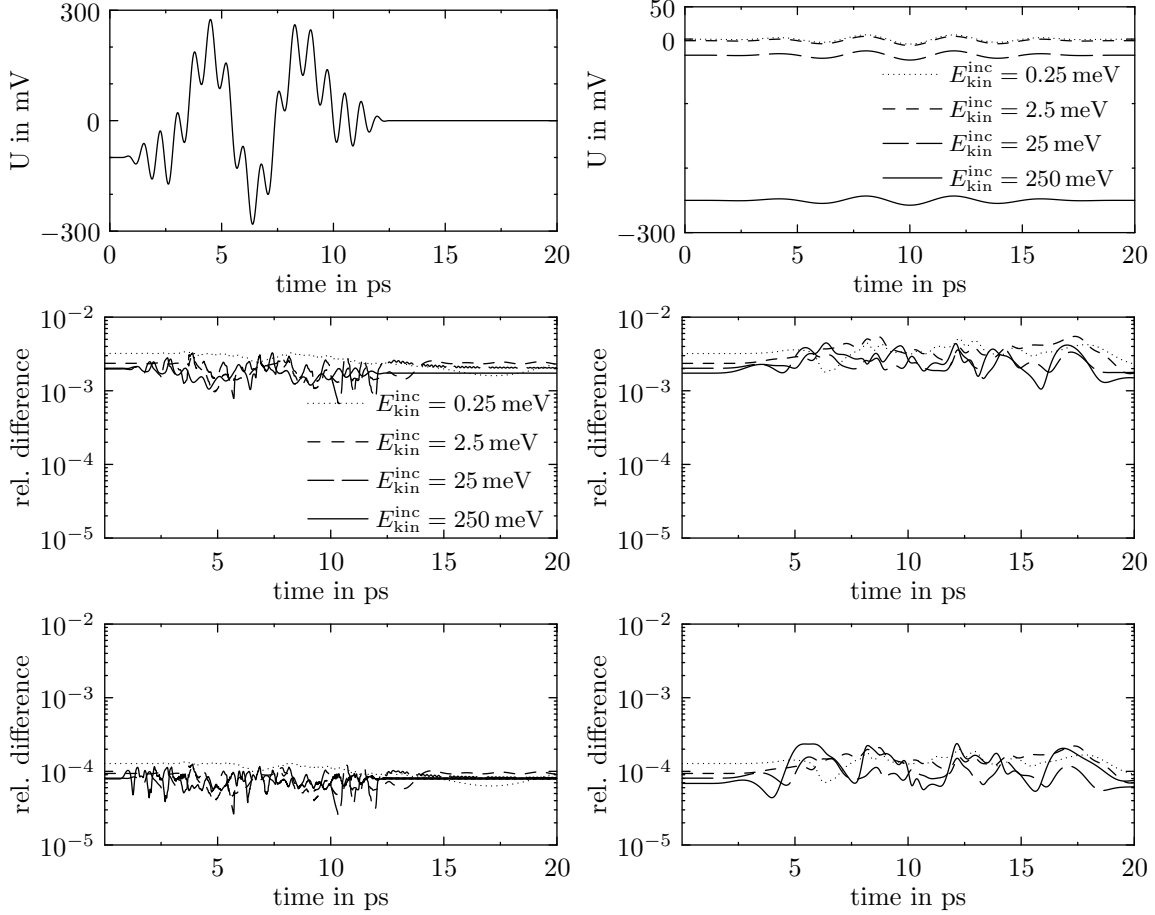


Figure 7: *Left column:* Relative differences between the solutions computed with DTBC and PML for $\Delta x = 0.5$ nm (center) or $\Delta x = 0.1$ nm (bottom) using the applied voltage $U(t)$ (top). The experiment is carried out four times corresponding to different values of $E_{\text{kin}}^{\text{inc}} = 0.25$ meV, 2.5 meV, 25 meV or 250 meV. *Right column:* Relative differences between the solutions computed with DTBC and PML for $\Delta x = 0.5$ nm (center) or $\Delta x = 0.1$ nm (bottom) using different applied voltages (top). The experiment is carried out four times corresponding to different values of $E_{\text{kin}}^{\text{inc}} = 0.25$ meV, 2.5 meV, 25 meV or 250 meV. In each simulation the applied voltage oscillates slowly around a different critical value $U = -0.25$ mV, -2.5 mV, -25 mV or -250 mV.

the PML. We repeat the experiment four times corresponding to different values of the kinetic energy $E_{\text{kin}}^{\text{inc}} = 0.25 \text{ meV}, 2.5 \text{ meV}, 25 \text{ meV}$ or 250 meV . The relative differences as a function of time are depicted in the left column of Figure 7 for $\Delta x = 0.5 \text{ nm}$ (center) or $\Delta x = 0.1 \text{ nm}$ (bottom).

In another four simulations, we let the applied voltage oscillate slowly around the critical values $U = -0.25 \text{ mV}, -2, 5 \text{ mV}, -25 \text{ mV}$ or -250 mV as depicted in the right column of Figure 7 (top). In this way, we trigger waves of arbitrary low energy in the right lead. The relative differences are depicted in the right column of Figure 7 for $\Delta x = 0.5 \text{ nm}$ (center) or $\Delta x = 0.1 \text{ nm}$ (bottom). It can be seen that the relative differences are always localized around a value of 3×10^{-3} , showing that PML can handle even the extreme cases.

3 Two-dimensional quantum waveguide simulations

3.1 Scattering states in quantum waveguides

We consider the stationary Schrödinger equation

$$\hat{H}\phi = E\phi, \quad \hat{H} = -\frac{\hbar^2}{2m^*}\Delta + V, \quad (34)$$

on the infinite strip $\Omega = \mathbb{R} \times (0, L_2)$ with homogeneous Dirichlet boundary conditions at $x_2 = 0$ and $x_2 = L_2$. For the quantum waveguide simulations, we assume that the potential energy in the exterior domain depends on the transversal coordinate only,

$$V(x_1, x_2) = \begin{cases} V_\ell(x_2) & \text{for } x_1 \leq 0, \\ V_r(x_2) & \text{for } x_1 \geq L_1. \end{cases}$$

In general, V_ℓ and V_r may be different, but to simplify the notation, we assume that $V_\ell(x_2) = V_r(x_2)$ for $x_2 \in [0, L_2]$. As an example, we refer to the ring-shaped device described by the potential energy shown in Figure 8.

We further assume that the wave function in the leads,

$$\phi(x_1, x_2) = \sum_{m=0}^{\infty} c^{(m)}(x_1) \chi^{(m)}(x_2), \quad x_1 \leq 0, \quad x_1 \geq L_1, \quad (35)$$

can be decomposed into transversal waveguide eigenstates,

$$-\frac{\hbar^2}{2m^*} \frac{\partial^2}{\partial x_2^2} \chi^{(m)}(x_2) + V(x_2) \chi^{(m)}(x_2) = E^{(m)} \chi^{(m)}(x_2), \quad \chi^{(m)}(0) = 0, \quad \chi^{(m)}(L_2) = 0, \quad (36)$$

$$\langle \chi^{(m)}, \chi^{(n)} \rangle = \int_0^{L_2} \chi^{(m)}(x_2) \overline{\chi^{(n)}(x_2)} dx_2 = \delta_{m,n},$$

where the mode coefficients $c^{(m)}(x_1) = \langle \phi(x_1, \cdot), \chi^{(m)} \rangle$ satisfy the one-dimensional stationary Schrödinger equation

$$-\frac{\hbar^2}{2m^*} \frac{\partial^2}{\partial x_1^2} c^{(m)}(x_1) + E^{(m)} c^{(m)}(x_1) = E c^{(m)}(x_1), \quad m \in \mathbb{N}_0. \quad (37)$$

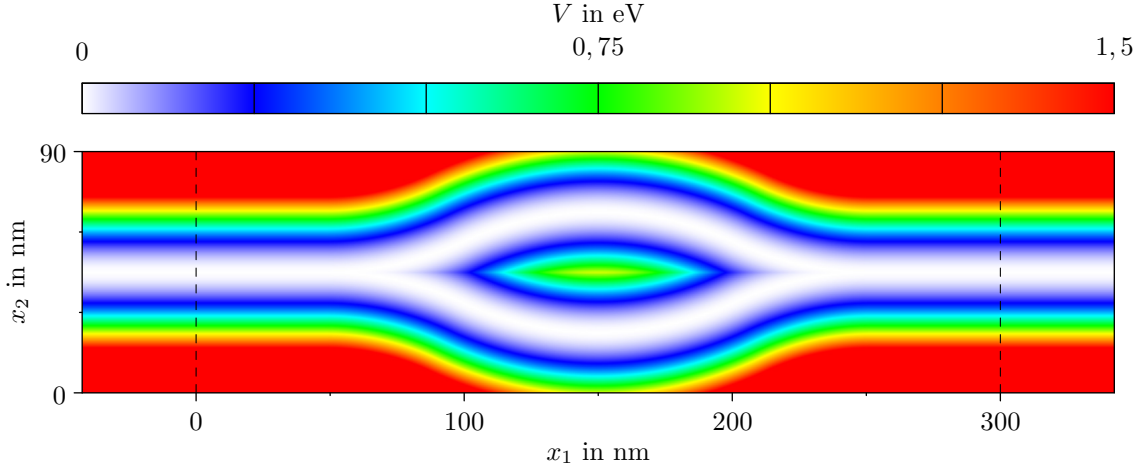


Figure 8: Potential energy of a ring-shaped quantum waveguide device. The device domain equals $[0, 300] \times [0, 90] \text{ nm}^2$.

In the following discussion, we consider electrons injected at the left terminal traveling to the right. Let their wave vector be given by $(k, 0)^\top$ with $k > 0$. At the time of the injection, the electrons are assumed to be in the ground state with respect to the cross section of the waveguide potential in the left lead. Hence, the incoming electrons are represented by

$$\phi^{\text{inc}}(x_1, x_2) := \exp(ikx_1)\chi^{(0)}(x_2), \quad (38)$$

and their total energy amounts to $E = E_{\text{kin}}^{\text{inc}} + E^{(0)}$, where $E_{\text{kin}}^{\text{inc}} = \hbar^2 k^2 / (2m^*)$.

Discrete transparent boundary conditions. The symmetric second-order finite-difference approximation of the spatial derivatives in (34) gives

$$-\frac{\hbar^2}{2m^*} \left(\frac{\phi_{j_1-1, j_2} - 2\phi_{j_1, j_2} + \phi_{j_1+1, j_2}}{(\Delta x)^2} + \frac{\phi_{j_1, j_2-1} - 2\phi_{j_1, j_2} + \phi_{j_1, j_2+1}}{(\Delta x)^2} \right) + V_{j_1, j_2} \phi_{j_1, j_2} = E \phi_{j_1, j_2} \quad (39)$$

on the semi-infinite grid $\Omega_{\Delta x} := \{(j_1 \Delta x, j_2 \Delta x) : j_1 \in \mathbb{Z}, j_2 = 0, \dots, J_2\}$, where $J_1 \Delta x = L_1$, $J_2 \Delta x = L_2$, and $\phi_{j_1, 0} = \phi_{j_1, J_2} = 0$ for all $j_1 \in \mathbb{Z}$. In particular, we seek for a solution of (39) restricted to the grid points of the device domain

$$\Omega_{\text{DTBC}} := \{(j_1 \Delta x, j_2 \Delta x) : j_1 = 0, \dots, J_1, j_2 = 0, \dots, J_2\},$$

where an incoming plane wave is prescribed at the left boundary. Disregarding open boundary conditions and the incoming plane wave, we can state the problem as

$$S\phi = 0, \quad \phi_j = \phi_{j_1, j_2}, \quad j = j_1 J_2 + j_2, \quad j_1 = 0, \dots, J_1, \quad j_2 = 0, \dots, J_2. \quad (40)$$

Here, S denotes the sparse matrix $S := -\hbar^2 / (2m^*) \Delta_{x_1, x_2}^{\text{2nd}} + \text{diag}(d)$, where $\Delta_{x_1, x_2}^{\text{2nd}} := D_{x_1}^{2, \text{2nd}} \otimes I_{J_2} + I_{J_1} \otimes D_{x_2}^{2, \text{2nd}}$. The components of the vector d are given by $d_j = V_j - E$, $j =$

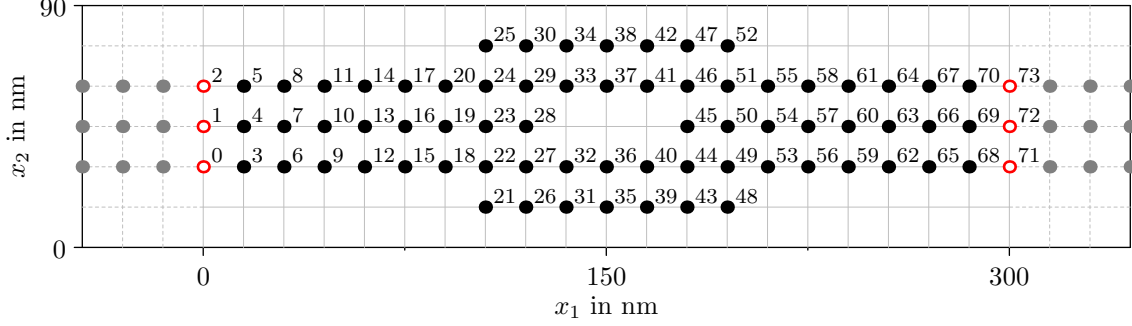


Figure 9: Reduced mesh of the ring shaped quantum device shown in Figure 8. For visualization purposes, Δx is chosen extremely large. Grid points at which the wave function is practically zero have been eliminated. For DTBC, the reduced mesh is given by the grid points between $x_1 = 0$ nm and $x_1 = 300$ nm. In case of PML, the reduced mesh contains also the grey points. In both cases, we prescribe an incoming plane wave at $x_1 = 0$ nm.

$0, \dots, (J_1 + 1)(J_2 + 1) - 1$, and I_{J_1}, I_{J_2} are unit matrices of dimension J_1 and J_2 , respectively. Finally, $D_{x_1}^{2,2\text{nd}}$ and $D_{x_2}^{2,2\text{nd}}$ are finite-difference matrices defined according to (13d) with respect to the two spatial directions x_1 and x_2 .

In order to realize discrete open boundary conditions at the device terminals, we need to replace those finite-difference equations in (40) which correspond to grid points at the left and right boundary of Ω_{DTBC} . Furthermore, some of the finite-difference equations can be eliminated because ϕ_j is zero due to the homogeneous Dirichlet boundary conditions imposed at the top and the bottom boundary of Ω_{DTBC} . In fact, we eliminate even more equations. Since the wave function ϕ_j decreases exponentially within areas where the potential energy is greater than the total energy of the electron, ϕ_j is zero (to numerical precision) at some distance from the center of the waveguide profile. This allows us to eliminate the corresponding finite-difference equations. More specifically, we eliminate all rows $S[j, :]$ and columns $S[:, j]$ of S with $j \in \{j : V_j > 750 \text{ meV}\}$. Through this elimination process, we implicitly obtain a reduced mesh and a new numbering of the remaining free indices. An illustration is given in Figure 9.

We still need to replace the remaining rows of S corresponding to grid points at the device contacts (open red points in Figure 9). Let us consider the left terminal first. Since the potential energy in the exterior domain depends solely on the transversal coordinate, we temporarily define $V_{j_2} := V_{j_1, j_2}$ for $j_1 \leq 0$ and $j_2 = 0, \dots, J_2$. Analogously to the continuous case, the wave function in the lead can be decomposed into transversal waveguide eigenstates:

$$\phi_{j_1, j_2} = \sum_{m=0}^{M-1} c_{j_1}^{(m)} \chi_{j_2}^{(m)}, \quad j_1 \leq 0, \quad j_2 = j_{21}, \dots, j_{22}.$$

The indices j_{21} and j_{22} depend on the elimination process described above. In the example of Figure 9, we have $j_{21} = 2$ and $j_{22} = 4$. Hence, the number of free indices along the

x_2 -direction in the left lead is given by $M = j_{22} - j_{21} + 1$. Further, $\chi^{(m)}$ denotes the m -th eigenstate of the discrete eigenvalue problem

$$-\frac{\hbar^2}{2m^*} \frac{\chi_{j_2-1}^{(m)} - 2\chi_{j_2}^{(m)} + \chi_{j_2+1}^{(m)}}{(\Delta x)^2} + V_{j_2} \chi_{j_2}^{(m)} = E^{(m)} \chi_{j_2}^{(m)}, \quad j_2 = j_{21}, \dots, j_{22}, \quad m = 0, \dots, M-1,$$

where we impose homogeneous Dirichlet boundary conditions at $x_2 = (j_{21} - 1)\Delta x$ and $x_2 = (j_{22} + 1)\Delta x$. We further ensure that all eigenstates are orthonormal with respect to the scalar product

$$\langle \chi^{(m)}, \chi^{(n)} \rangle = \Delta x \sum_{j_2=j_{21}}^{j_{22}} \chi_{j_2}^{(m)} \overline{\chi_{j_2}^{(n)}}. \quad (41)$$

The ground state ($m = 0$) and the first excited state ($m = 1$) are shown in Figure 10 (left).

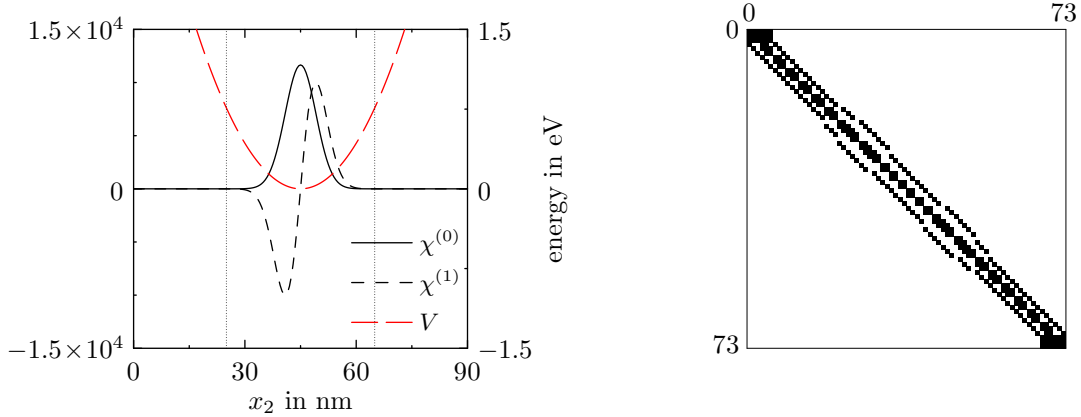


Figure 10: *Left*: Ground state and first excited eigenstate corresponding to the cross-sectional potential energy in the left lead of the quantum waveguide depicted in Figure 8. The vertical dotted lines indicate the boundaries of the reduced mesh. *Right*: Sparsity pattern of S corresponding to the example considered in Figure 9.

In the continuous case, the coefficients $c^{(m)}$ solve (37) for all $m \in \mathbb{N}_0$. The discrete analogue of (37) reads as

$$-\frac{\hbar^2}{2m^*} \frac{c_{j_1-1}^{(m)} - 2c_{j_1}^{(m)} + c_{j_1+1}^{(m)}}{(\Delta x)^2} + E^{(m)} c_{j_1}^{(m)} = E c_{j_1}^{(m)}, \quad m = 0, \dots, M-1, \quad (42)$$

which can be identified with the one-dimensional discrete stationary Schrödinger equation (3) if the potential energy is substituted by $E^{(m)}$. Thus, (42) admits two solutions of the form $c_{j_1}^{(m)} = (\alpha^{(m)})^{j_1}$, where

$$\alpha^{(m)} = 1 - \frac{m^*(E - E^{(m)})(\Delta x)^2}{\hbar^2} \pm i \sqrt{\frac{2m^*(E - E^{(m)})(\Delta x)^2}{\hbar^2} - \frac{(m^*)^2(E - E^{(m)})^2(\Delta x)^4}{\hbar^4}}.$$

Recall that m denotes the mode index and m^* the effective mass of the electron and that we consider electrons which are injected at the left terminal traveling to the right. At the time of the injection, the electrons are assumed to be in the ground state with respect to the waveguide profile. Thus, we have

$$c_{j_1}^{(0)} = A(\alpha^{(0)})^{j_1} + B(\alpha^{(0)})^{-j_1},$$

where A and B are the amplitudes of the incoming and the reflected wave projected to the ground state $\chi^{(0)}$, respectively. Writing the above equation for $j_1 = 0, 1$ and eliminating B yields

$$c_0^{(0)} - \alpha^{(0)}c_1^{(0)} = A(1 - (\alpha^{(0)})^2), \quad (43)$$

which corresponds to equation (5) with $A = 1$. Here, we use $A = 1/\Delta x$ which gives a reasonable scaling of the final wave function. In other words, the final wave function will be of the same order as the transversal waveguide eigenstates. In case of the excited modes ($m > 0$), the amplitude of the incoming wave is zero. Thus, we have

$$c_0^{(m)} - \alpha^{(m)}c_1^{(m)} = 0, \quad m = 1, \dots, M - 1. \quad (44)$$

Again, the mode coefficients are the projections of the wave function onto the transversal waveguide eigenstates. More precisely, using the scalar product (41) and the fact that all eigenstates are real-valued, we can write the discrete analogue of $c^{(m)}$ solving (37) as

$$c_{j_1}^{(m)} = \Delta x \sum_{j_2=j_{21}}^{j_{22}} \phi_{j_1, j_2} \chi_{j_2}^{(m)}, \quad m = 0, \dots, M - 1. \quad (45)$$

The remaining free indices corresponding to the grid points at the left boundary of the device are $0, \dots, M - 1$. Furthermore, the free indices of the adjacent grid points are $M, \dots, 2M - 1$ (see Figure 9). Thus, using (43), (44), and (45), DTBC at $x_1 = 0$ become

$$\left(\Delta x \sum_{j=0}^{M-1} \phi_j \chi_j^{(m)} \right) - \alpha^{(m)} \left(\Delta x \sum_{j=M}^{2M-1} \phi_j \chi_j^{(m)} \right) = \frac{1}{\Delta x} (1 - (\alpha^{(0)})^2) \delta_{m,0}, \quad (46)$$

for all $m = 0, \dots, M - 1$. Each of these M equations is used to replace one equation corresponding to a grid point at the left boundary of the reduced mesh. In other words, we replace the first M rows of S according to the left-hand side of (46).

DTBC at $x_1 = L_1$ follow analogously. Since we do not prescribe an incoming wave at the right contact, the inhomogeneity does not show up, leading to

$$\left(\Delta x \sum_{j=N-M}^{N-1} \phi_j \chi_j^{(m)} \right) - \alpha^{(m)} \left(\Delta x \sum_{j=N-2M}^{N-M-1} \phi_j \chi_j^{(m)} \right) = 0, \quad m = 0, \dots, M - 1. \quad (47)$$

The last M rows of S are replaced according to (47) which finally yields

$$S\phi = b, \quad \phi = (\phi_0, \dots, \phi_{N-1})^\top, \quad b = (b_0, \dots, b_{N-1})^\top, \quad (48)$$

where $b_j = (1/\Delta x)(1 - (\alpha^{(0)})^2)\delta_{j,0}$.

In some numerical experiments we noticed that the condition number of S is quite large. This problem can be easily overcome by scaling all equations (apart from the ones given in (46) and (47)) with $1/E$. The sparsity pattern of S is depicted in Figure 10. Obviously, S contains two dense submatrices which are a direct consequence of the DTBC (46) and (47). For that reason, the symmetry of S is lost and consequently, many iterative methods cannot be applied to solve (48). However, the simulations considered below can still be handled by direct solvers and we are not affected by the loss of symmetry of S .

Perfectly Matched Layers. Similarly to the one-dimensional case, we replace the Laplacian in the stationary Schrödinger equation by the Laplace-PML operator

$$\frac{\partial^2}{\partial x_1^2} + \frac{\partial^2}{\partial x_2^2} \rightarrow c(x_1) \frac{\partial}{\partial x_1} c(x_1) \frac{\partial}{\partial x_1} + \frac{\partial^2}{\partial x_2^2}, \quad (49)$$

which yields the stationary Schrödinger-PML equation

$$-\frac{\hbar^2}{2m^*} \left(c(x_1) \frac{\partial}{\partial x_1} c(x_1) \frac{\partial}{\partial x_1} + \frac{\partial^2}{\partial x_2^2} \right) \phi(x_1, x_2) + V(x_1, x_2) \phi(x_1, x_2) = E \phi(x_1, x_2). \quad (50)$$

We choose the same function $c(x)$ as in Section 2.1.

According to (12a), a second-order finite-difference discretization of (50) is given by

$$-\frac{\hbar^2}{2m^*} \left(c(x_{j_1}) c'(x_{j_1}) \frac{-\phi_{j_1-1, j_2} + \phi_{j_1+1, j_2}}{2\Delta x} + c^2(x_{j_1}) \frac{\phi_{j_1-1, j_2} - 2\phi_{j_1, j_2} + \phi_{j_1+1, j_2}}{(\Delta x)^2} \right. \\ \left. + \frac{\phi_{j_1, j_2-1} - 2\phi_{j_1, j_2} + \phi_{j_1, j_2+1}}{(\Delta x)^2} \right) + V_{j_1, j_2} \phi_{j_1, j_2} = E \phi_{j_1, j_2}, \quad j_1 \in \mathbb{Z}, \quad j_2 = 0, \dots, J_2.$$

In fact, we seek for a solution restricted to the computational domain

$$\Omega_{\text{PML}} = \{ (X_{j_1}^{\text{PML}}, j_2 \Delta x) : j_1 = 0, \dots, J_1^{\text{PML}}, j_2 = 0, \dots, J_2 \},$$

where $X_{j_1}^{\text{PML}}$ denotes the j_1 -th grid point of the one-dimensional grid X_{PML} defined in (14). Without taking into account a possible incoming plane wave, we can state the problem in the following form:

$$S_{\text{PML}} \phi = 0, \quad \phi_j = \phi_{j_1, j_2}, \quad j = j_1 J_2 + j_2, \quad j_1 = 0, \dots, J_1^{\text{PML}}, \quad j_2 = 0, \dots, J_2.$$

where $S_{\text{PML}} := -\hbar^2/(2m^*) \tilde{\Delta}_{x_1, x_2} + \text{diag}(d)$, and $\tilde{\Delta}_{x_1, x_2}$ is one of the sparse matrices

$$\tilde{\Delta}_{x_1, x_2}^{\text{2nd}} := \left(\tilde{D}_{x_1}^{\text{2,2nd}} \otimes I_{J_2} + I_{J_1^{\text{PML}}} \otimes D_{x_2}^{\text{2,2nd}} \right), \quad (51a)$$

$$\tilde{\Delta}_{x_1, x_2}^{\text{4th}} := \left(\tilde{D}_{x_1}^{\text{2,4th}} \otimes I_{J_2} + I_{J_1^{\text{PML}}} \otimes D_{x_2}^{\text{2,4th}} \right), \quad (51b)$$

$$\tilde{\Delta}_{x_1, x_2}^{\text{6th}} := \left(\tilde{D}_{x_1}^{\text{2,6th}} \otimes I_{J_2} + I_{J_1^{\text{PML}}} \otimes D_{x_2}^{\text{2,6th}} \right), \quad (51c)$$

corresponding to second-, fourth-, and sixth-order discretizations of the Laplace-PML operator (49). The finite-difference matrices corresponding to the x_1 -direction are defined via (12) and the finite-difference matrices acting on the x_2 -direction are given in (13d)-(13f). Finally, the vector d is defined via $d_j = V_j - E$, $j = 0, \dots, (J_1^{\text{PML}} + 1)(J_2 + 1) - 1$.

Before we realize an incoming plane wave at the left terminal, we eliminate all finite-difference equations corresponding to grid points where the wave function is supposed to be zero. Like in the case of DTBC, we eliminate all rows $S_{\text{PML}}[j, :]$ and columns $S_{\text{PML}}[:, j]$ of S_{PML} with $j \in \{j : V_j > 750 \text{ meV}\}$. Let $N_{\text{PML}} \times N_{\text{PML}}$ denote the new size of S_{PML} . The elimination process implicitly yields a reduced mesh which extends the reduced mesh considered in the case of DTBC (see Figure 9). The wave function in the left contact is a superposition of an incoming and a reflected wave, $\phi_{j_1, j_2} = \phi_{j_1, j_2}^{\text{inc}} + \phi_{j_1, j_2}^{\text{refl}}$. The incoming wave

$$\phi_{j_1, j_2}^{\text{inc}} = \chi_{j_2}^{(0)} \exp(ikj_1 \Delta x), \quad j_1 \leq 0, \quad j_2 = j_{21}, \dots, j_{22}, \quad (52)$$

is a discrete representation of (38), where $\chi^{(0)}$ is a solution of

$$-\frac{\hbar^2}{2m^*} D_{x_2}^2 \chi_{j_2}^{(0)} + V_{j_2} \chi_{j_2}^{(0)} = E^{(0)}, \quad D_{x_2}^2 \in \{D_{x_2}^{2,2\text{nd}}, D_{x_2}^{2,4\text{th}}, D_{x_2}^{2,6\text{th}}\}, \quad j_2 = j_{21}, \dots, j_{22}.$$

Like in the case of DTBC, we impose homogeneous Dirichlet boundary conditions at $x_2 = (j_{21} - 1)\Delta x$ and $x_2 = (j_{22} + 1)\Delta x$. The wave number k is related to the kinetic energy $E_{\text{kin}}^{\text{inc}}$ according to the discrete E - k -relation (7). In case of the higher-order methods, we simply use the continuous relation (6). Let again M denote the number of free indices along the x_2 -direction in the left lead. Moreover, let $j_0, \dots, j_0 + M - 1$ denote the free indices of the grid points at $x_1 = 0$ with respect to the reduced mesh ($j_0 = 9$ in Figure 9). With these notations, an incoming plane wave is realized in the same way as in the one-dimensional case. For the second-order discretization, we find that

$$S_{\text{PML}} \phi = b, \quad \phi = (\phi_0, \dots, \phi_{N_{\text{PML}}-1})^\top, \quad b = (b_0, \dots, b_{N_{\text{PML}}-1})^\top,$$

where

$$b_j = \begin{cases} -\frac{\hbar^2}{2m^*(\Delta x)^2} \phi_{j+M}^{\text{inc}} & \text{for } j = j_0 - M, \dots, j_0 - 1, \\ +\frac{\hbar^2}{2m^*(\Delta x)^2} \phi_{j-M}^{\text{inc}} & \text{for } j = j_0, \dots, j_0 + M - 1, \\ 0 & \text{else.} \end{cases}$$

In case of the higher-order discretizations, b needs to be adapted accordingly.

Since S_{PML} does not contain dense submatrices, it can be assembled more easily than the corresponding matrix in (48). However, depending on the ratio between the number of grid points needed to describe the device domain and the number of grid points needed to realize the PML, the size of S_{PML} may be significantly larger than that of S in (48). Moreover, S_{PML} is not Hermitian. Thus, like in the case of DTBC, many iterative methods cannot be applied.

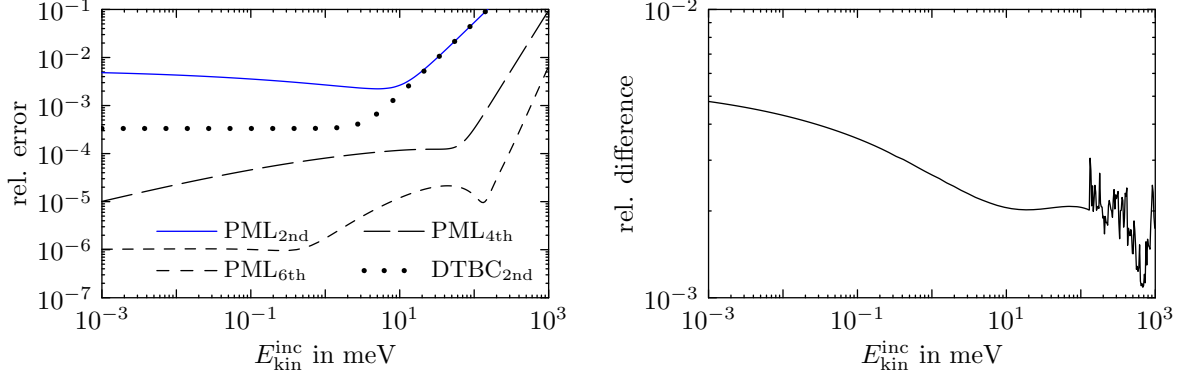


Figure 11: *Left:* Relative errors as a function of $E_{\text{kin}}^{\text{inc}}$ in a numerical scattering state experiment. The electrons are injected at the left contact of a straight waveguide with parabolic cross section. *Right:* Relative differences between the solutions obtained by PML_{2nd} and DTBC_{2nd} as a function of $E_{\text{kin}}^{\text{inc}}$. The electrons are injected at the left terminal of the ring-shaped waveguide depicted in Figure 8.

Simulations. Before we turn our attention to the ring-shaped quantum device introduced above, let us first consider a straight waveguide with parabolic cross section, i.e.,

$$V(x_1, x_2) = \frac{1}{2} m^* \omega_*^2 \left(x_2 - \frac{L_2}{2} \right)^2, \quad \omega_* = 0.5 \times 10^{14} \text{ s}^{-1}, \quad x_1 \in \mathbb{R}, \quad x_2 \in [0, L_2]. \quad (53)$$

The cross-sectional eigenstates and eigenvalues read as

$$\begin{aligned} \chi^{(n)}(x_2) &= \left(\frac{m^* \omega_*}{\pi \hbar} \right)^{1/4} \frac{1}{\sqrt{2^n n!}} H_n \left(\sqrt{\frac{m^* \omega_*}{\hbar}} \left(x_2 - \frac{L_2}{2} \right) \right) \\ &\times \exp \left(-\frac{1}{2} \frac{m^* \omega_*}{\hbar} \left(x_2 - \frac{L_2}{2} \right)^2 \right), \quad E^{(n)} = \hbar \omega_* \left(n + \frac{1}{2} \right), \quad n \in \mathbb{N}_0, \end{aligned} \quad (54)$$

where H_n denote the Hermite polynomials.

In this trivial example, the solution of the scattering state problem is given by (38), where $\chi^{(0)}$ is substituted according to (54). We compare the exact solution with the results of the different numerical solvers using the mesh size $\Delta x = 0.5$ nm. To this end, we set $[0, L_1] \times [0, L_2] = [0, 120] \times [0, 60]$ nm². The relative errors are depicted in Figure 11 (left) for the energy range $E_{\text{kin}}^{\text{inc}} \in [10^{-3}, 10^3]$ meV. As expected, the results resemble the results from the corresponding one-dimensional simulation (Figure 2 right). However, while in the one-dimensional simulation, the errors of DTBC_{2nd} are decreasing continuously for decreasing $E_{\text{kin}}^{\text{inc}}$, they are now bounded from below. This lower bound results from the finite numerical resolution of the transversal waveguide eigenstate $\chi^{(0)}$.

We now consider the ring-shaped quantum device depicted in Figure 8. A scattering state solution according to PML_{2nd} is shown in Figure 12 for $E_{\text{kin}}^{\text{inc}} = 21.5$ meV. Here and in all subsequent figures, the wave function is scaled by the maximum of the transversal

waveguide eigenstate $\chi^{(0)}$. As can be seen, the electrons are transmitted almost perfectly through the device. Hence, the reflected wave in the left terminal is practically zero.

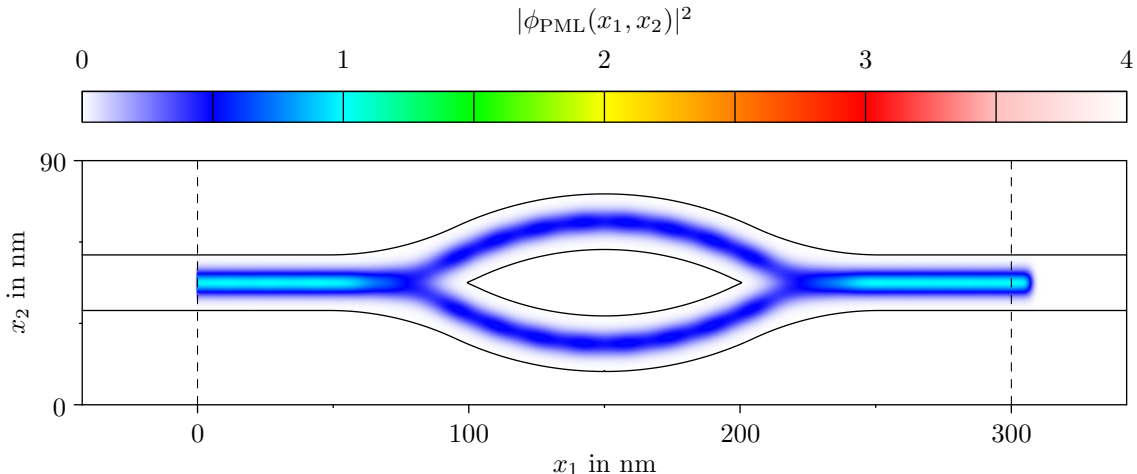


Figure 12: Scattering state in the ring-shaped quantum waveguide shown in Figure 8. The kinetic energy of the electrons injected at the left contact is $E_{\text{kin}}^{\text{inc}} = 21.5$ meV. The black solid line indicates an isoline of the potential energy at 200 meV.

Next, we compute scattering state solutions for the energy range $E_{\text{kin}}^{\text{inc}} \in [10^{-3}, 10^3]$ meV. Since exact solutions are not available and our solver using DTBC is restricted to second-order accuracy, we only compare the solutions corresponding to $\text{DTBC}_{2\text{nd}}$ and $\text{PML}_{2\text{nd}}$. Their relative differences at a spatial resolution of $\Delta x = 0.5$ nm are given in Figure 11 (right). For energies up to approximately 100 meV, the results are consistent with the results shown in Figure 11 (left). For larger energies, the small wavelength of the wave function can hardly be resolved with second-order methods. Nonetheless, $\text{DTBC}_{2\text{nd}}$ and $\text{PML}_{2\text{nd}}$ yield approximately the same results, even though the relative differences vary considerably.

Finally, we compute the transmission probability as a function of the kinetic energy of the incident electrons. The transmission probability is defined as the ratio between the transmitted and the incident probability current density [13]. In the given situation (provided $E_{\text{kin}}^{\text{inc}}$ is not too large) we have

$$\frac{j_{\text{trans}}}{j_{\text{inc}}} = |\langle \phi(L_1, \cdot), \chi^{(0)} \rangle|^2, \quad (55)$$

which is depicted in Figure 13.

3.2 Transient scattering states in quantum waveguides

We consider the time-dependent Schrödinger equation

$$i\hbar\partial_t\psi = \hat{H}\psi, \quad \hat{H} = -\frac{\hbar^2}{2m^*}\Delta + V \quad (56)$$

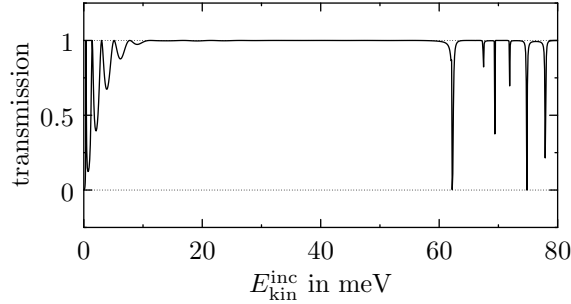


Figure 13: Transmission probability as a function of $E_{\text{kin}}^{\text{inc}}$ for electrons injected at the left terminal of the ring-shaped device shown in Figure 8.

on the infinite strip $\Omega = \mathbb{R} \times (0, L_2)$. Like in the stationary case, we prescribe homogeneous Dirichlet boundary conditions at $x_2 = 0$ and $x_2 = L_2$. Moreover, we assume that $V(x_1, x_2, t) = V(x_2)$ for $x_1 \leq 0$ or $x_1 \geq L_1$ and $x_2 \in [0, L_2]$. This condition is satisfied for the potential in Figure 8. In many applications, the potentials in the left and right lead are not necessarily the same. Furthermore, they may depend on time via an applied voltage, e.g. $V(x_1, x_2, t) = V(x_2) - eU(t)$. These extensions can be easily included in the following discussion using the results from Section 2.

In the transient scattering state experiment, the initial wave function is given by a scattering state solution of the stationary Schrödinger equation for the potential energy $V(x_1, x_2, 0)$ and the total energy $E = E_{\text{kin}}^{\text{inc}} + E^{(0)}$, where $E_{\text{kin}}^{\text{inc}} = \hbar^2 k^2 / (2m^*)$.

Using time-dependent mode coefficients, the wave function in the leads can still be decomposed into transversal waveguide eigenstates (36),

$$\psi(x_1, x_2, t) = \sum_{m=0}^{\infty} d^{(m)}(x_1, t) \chi^{(m)}(x_2), \quad x_1 \leq 0, \quad x_1 \geq L_1. \quad (57)$$

Substituting (57) into (56) shows that each coefficient satisfies the one-dimensional time-dependent Schrödinger equation

$$i\hbar \frac{\partial}{\partial t} d^{(m)}(x_1, t) = -\frac{\hbar^2}{2m^*} \frac{\partial^2}{\partial x_1^2} d^{(m)}(x_1, t) + E^{(m)} d^{(m)}(x_1, t), \quad t \geq 0, \quad m \in \mathbb{N}_0. \quad (58)$$

As an eigenstate of the Schrödinger equation, the scattering state evolves in time according to $\exp(-i\omega t)$ with $\omega = E/\hbar$. Hence, the time-evolution of the scattering state in the leads is given by

$$\sum_{m=0}^{\infty} \exp(-iEt/\hbar) c^{(m)}(x_1) \chi^{(m)}(x_2), \quad x_1 \leq 0, \quad x_1 \geq L_1,$$

where $e^{(m)}(x_1, t) := \exp(-iEt/\hbar) c^{(m)}(x_1)$ solves (58) as well. Hence, $\exp(iE^{(m)}t/\hbar) d^{(m)}$ and $\exp(iE^{(m)}t/\hbar) e^{(m)}$ solve the free time-dependent one-dimensional Schrödinger equation and

therefore transparent boundary conditions at $x_1 = 0$ and $x_1 = L_1$ can be derived by the application of (19) to

$$\exp(iE^{(m)}t/\hbar)d^{(m)} - \exp(iE^{(m)}t/\hbar)e^{(m)} \quad (59)$$

for each $m \in \mathbb{N}_0$.

Discrete transparent boundary conditions. Using the same grid Ω_{DTBC} as in the stationary case, we formulate the Crank-Nicolson scheme for the two-dimensional time-dependent Schrödinger equation (56) as follows:

$$P\psi^{(n+1)} = Q\psi^{(n)}, \quad \psi_j^{(n)} = \psi_{j_1, j_2}^{(n)}, \quad j = j_1 J_2 + j_2, \quad (60)$$

where $j_1 = 0, \dots, J_1$, $j_2 = 0, \dots, J_2$, $n \in \mathbb{N}_0$, P and Q are the sparse matrices

$$\begin{aligned} P &:= I - \frac{i\Delta t\hbar}{4m^*} \Delta_{x_1, x_2}^{\text{2nd}} + \frac{i\Delta t}{2\hbar} \text{diag} \left((V_0^{(n+1/2)}, \dots, V_{J_1 J_2 - 1}^{(n+1/2)})^\top \right), \\ Q &:= I + \frac{i\Delta t\hbar}{4m^*} \Delta_{x_1, x_2}^{\text{2nd}} - \frac{i\Delta t}{2\hbar} \text{diag} \left((V_0^{(n+1/2)}, \dots, V_{J_1 J_2 - 1}^{(n+1/2)})^\top \right). \end{aligned}$$

As outlined in Section 3.1, we eliminate all finite-difference equations corresponding to grid points at which the wave function is zero. Needless to say, we eliminate the same rows and columns of P and Q which have been eliminated in S (see Section 3.1). Using the same notations as in Section 3.1, the wave function in the leads of the reduced mesh reads as

$$\psi_{j_1, j_2}^{(n)} = \sum_{m=0}^{M-1} d_{j_1}^{(m, n)} \chi_{j_2}^{(m)}, \quad j_1 \leq 0, \quad j_1 \geq J_1, \quad j_2 = j_{21}, \dots, j_{22}.$$

In order to derive DTBC at $x_1 = 0$ and $x_1 = L_1$, we employ the same strategy as in the continuous case considered above. The discrete analogue of (59) becomes

$$\epsilon^{(m, n)} d_{j_1}^{(m, n)} - \gamma^{(m, n)} c_{j_1}^{(m)}, \quad (61)$$

where the discrete gauge change terms

$$\begin{aligned} \epsilon^{(m, n)} &= \exp(2in \arctan(\Delta t E^{(m)}/(2\hbar))) \approx \exp(iE^{(m)}t/\hbar), \\ \gamma^{(m, n)} &= \exp(2in(\arctan(\Delta t E^{(m)}/(2\hbar)) - \arctan(\Delta t E/(2\hbar)))) \\ &\approx \exp(iE^{(m)}t/\hbar) \exp(-iEt/\hbar), \quad m = 0, \dots, M-1, \quad n \in \mathbb{N}_0, \end{aligned}$$

are slight modifications of (33). Applying (23a) and (23b) to (61) yields the DTBC

$$\begin{aligned} \epsilon^{(m, n+1)} d_1^{(m, n+1)} - s^{(0)} \epsilon^{(m, n+1)} d_0^{(m, n+1)} &= \sum_{\ell=1}^n s^{(n+1-\ell)} (\epsilon^{(m, \ell)} d_0^{(m, \ell)} - \gamma^{(m, \ell)} c_0^{(m)}) \\ &\quad - (\epsilon^{(m, n)} d_1^{(m, n)} - \gamma^{(m, n)} c_1^{(m)}) + \gamma^{(m, n+1)} c_1^{(m)} - s^{(0)} \gamma^{(m, n+1)} c_0^{(m)}, \end{aligned} \quad (62a)$$

$$\begin{aligned} \epsilon^{(m, n+1)} d_{J_1-1}^{(m, n+1)} - s^{(0)} \epsilon^{(m, n+1)} d_{J_1}^{(m, n+1)} &= \sum_{\ell=1}^n s^{(n+1-\ell)} (\epsilon^{(m, \ell)} d_{J_1}^{(m, \ell)} - \gamma^{(m, \ell)} c_{J_1}^{(m)}) \\ &\quad - (\epsilon^{(m, n)} d_{J_1-1}^{(m, n)} - \gamma^{(m, n)} c_{J_1-1}^{(m)}) + \gamma^{(m, n+1)} c_{J_1-1}^{(m)} - s^{(0)} \gamma^{(m, n+1)} c_{J_1}^{(m)} \end{aligned} \quad (62b)$$

at the left and right contact, respectively. The mode coefficients appearing on the left-hand side of (62) are implicitly given by the projection of the new wave function onto the transversal waveguide eigenstates

$$\begin{aligned} d_0^{(m,n+1)} &= \Delta x \sum_{j=0}^{M-1} \psi_j^{(n+1)} \chi_j^{(m)}, & d_1^{(m,n+1)} &= \Delta x \sum_{j=M}^{2M-1} \psi_j^{(n+1)} \chi_j^{(m)}, \\ d_{J_1-1}^{(m,n+1)} &= \Delta x \sum_{j=N-2M}^{N-M-1} \psi_j^{(n+1)} \chi_j^{(m)}, & d_{J_1}^{(m,n+1)} &= \Delta x \sum_{j=N-M}^{N-1} \psi_j^{(n+1)} \chi_j^{(m)}. \end{aligned}$$

Finally, all remaining equations in (60), which correspond to grid points at the left and right device contacts, are replaced. In the particular example of the reduced mesh shown in Figure 9, the first M equations are replaced according to (62a) and the last M equations are replaced according to (62b). The left-hand sides of (62) cause dense submatrices in P which need to be updated in each time step. All quantities appearing on the right-hand side of (62) are already known (at the n -th time step) or can be easily computed. However, to be able to perform the next time step, we need to store all values of $d_0^{(m,\ell)}$ and $d_{J_1}^{(m,\ell)}$ for $m = 0, \dots, M-1$ and $\ell = 1, \dots, n$. Hence, the storage requirements for the DTBC are in $O(Mn_\star)$, where n_\star denotes the total number of time steps. Furthermore, the computational time required for a single evaluation of the discrete convolutions in (62) increases linearly with n and thus, the total time complexity is in $O(Mn_\star^2)$.

Perfectly Matched Layers. Substituting the Laplacian in the time-dependent Schrödinger equation with the Laplace-PML operator (49) gives the time-dependent Schrödinger-PML equation for $\psi = \psi(x_1, x_2, t)$:

$$i\hbar \frac{\partial \psi}{\partial t} = -\frac{\hbar^2}{2m^\star} \left(c(x_1) \frac{\partial}{\partial x_1} c(x_1) \frac{\partial}{\partial x_1} + \frac{\partial^2}{\partial x_2^2} \right) \psi + V(x_1, x_2, t) \psi.$$

The semi-discretized problem on Ω_{PML} reads as

$$\frac{d}{dt} \psi_j(t) = i \frac{\hbar}{2m^\star} \tilde{\Delta}_{x_1, x_2} \psi_j(t) - \frac{i}{\hbar} V(t) \psi_j(t), \quad \psi_j(t) = \psi_{j_1, j_2}(t),$$

where $j = j_1 J_2 + j_2$, $j_1 = 0, \dots, J_1^{\text{PML}}$, $j_2 = 0, \dots, J_2$, and $\tilde{\Delta}_{x_1, x_2}$ denotes one of the sparse matrices defined in (51). For the time-integration method, we employ the Crank-Nicolson scheme (21) or the classical Runge-Kutta method. Like in the stationary case, we eliminate all equations corresponding to grid points at which the wave function is assumed to be zero. The incoming plane wave (52) used in the stationary problem becomes time-dependent, i.e., it is multiplied by $\exp(-i\omega n \Delta t)$. In case of the second-order discretization, ω is related to the total energy E according to (28). Otherwise we simply use $\omega = E/\hbar$. A time-dependent incoming wave can be included analogously to the one-dimensional case outlined in Section 2.3. In particular, we refer to the modifications in (29). For the sake of brevity, we omit the details. The storage requirements for the PML are in $O(MJ_1^\star)$, where

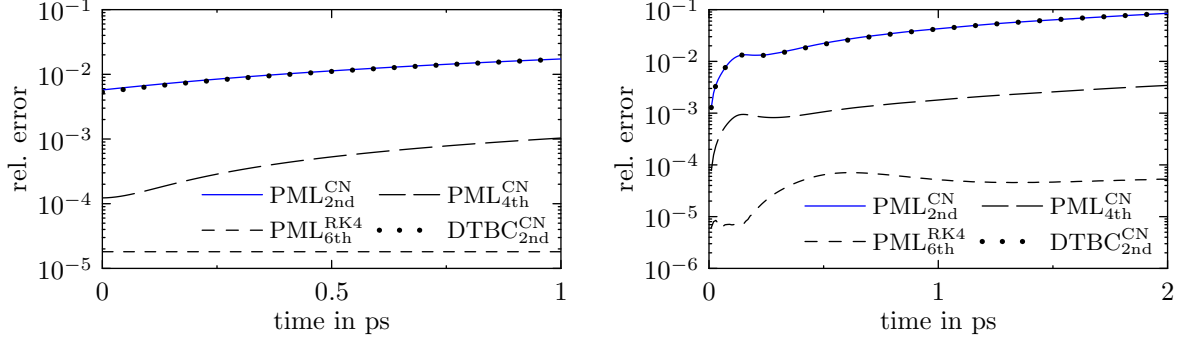


Figure 14: *Left:* Relative errors of the numerical solutions as a function of time in a transient scattering state experiment. *Right:* Time evolution of the numerical errors corresponding to two superimposed wave packets in a straight waveguide with parabolic cross section.

J_1^* denotes the number of indices j_1 with $X_{j_1}^{\text{PML}} < 0$ or $X_{j_1}^{\text{PML}} > L_1$. Contrary to DTBC, the computational time required to perform one time step is constant.

Simulations. In the simple example of the straight waveguide (53), the solution of the transient scattering state problem outlined above is given by

$$\psi(x_1, x_2, t) = \exp(ikx_1 - i\omega t)\chi^{(0)}(x_2),$$

where $\omega = E/\hbar$, $E = E_{\text{kin}}^{\text{inc}} + E^{(0)}$, $E_{\text{kin}}^{\text{inc}} = \hbar^2 k^2 / (2m^*)$. Here, $\chi^{(0)}$ and $E^{(0)}$ are substituted according to (54). We compare the exact solution with the results of the different numerical solvers. For this, we set $[0, L_1] \times [0, L_2] = [0, 120] \times [0, 60] \text{ nm}^2$. The kinetic energy of the incoming electrons is $E_{\text{kin}}^{\text{inc}} = 21.5 \text{ meV}$. For the time-integration, we either employ the Crank-Nicolson method or the classical Runge-Kutta method. In the former case, we use $\Delta x = 0.5 \text{ nm}$ and $\Delta t = 0.25 \text{ fs}$. We note that this choice is rather expensive since a linear system of equations has to be solved in each time step. For the Runge-Kutta method, we use the same spatial mesh size but a smaller time step size of $\Delta t \lesssim 0.05 \text{ fs}$ is needed to ensure stability. However, despite of this small time step size, the computation times are the shortest compared to those of all other employed solvers. The relative errors are shown in Figure 14 (left).

The numerical methods derived above can be easily modified to allow for simulations of wave packets in quantum waveguides. For instance, to simulate wave packets using the solver corresponding to DTBC, we set $c_0^{(m)} = c_1^{(m)} = c_{j_1-1}^{(m)} = c_{j_1}^{(m)} = 0$ in (62) for all $m = 0, \dots, M - 1$. In case of PML, we simply omit the incoming wave at the device contact.

In the following experiment, we consider the time evolution of two superimposed wave packets in the straight waveguide with parabolic cross section. More precisely, we start the numerical calculations using the exact solution

$$\psi(x_1, x_2, t) := \xi_p(x_1, t) \exp(-iE^{(0)}t/\hbar)\chi^{(0)}(x_2) + \xi_p(x_1, t) \exp(-iE^{(1)}t/\hbar)\chi^{(1)}(x_2),$$

at $t = 0$ ps, where ξ_p is defined in (25) with the parameters $\sigma = 7.5$ nm, $x_0 = L_1/2$, and $k_p = \sqrt{2m^* 21.5 \text{ meV}/\hbar}$. The transversal waveguide eigenstates and eigenvalues are defined in (54). We set $[0, L_1] \times [0, L_2] = [0, 160] \times [0, 60] \text{ nm}^2$.

The relative errors are depicted in Figure 14 (right). We see that $\text{DTBC}_{2\text{nd}}^{\text{CN}}$ and $\text{PML}_{2\text{nd}}^{\text{CN}}$ yield very similar results which is in contrast to the one-dimensional results shown in Figure 4. In this simulation, the wave packet is confined to a narrow channel and consequently, the wave function does not only oscillate in the longitudinal direction but also in the vertical direction. For the given cross section of the waveguide (characterized by $\omega_* = 0.5 \times 10^{14} \text{ s}^{-1}$), we find $E^{(0)} \approx 16.45 \text{ meV}$ and $E^{(1)} \approx 49.36 \text{ meV}$. The oscillation corresponding to the second energy cannot be easily resolved by second-order methods at the given spatio-temporal resolution. As a consequence, the discretization of the boundary conditions plays a minor role and thus $\text{DTBC}_{2\text{nd}}^{\text{CN}}$ and $\text{PML}_{2\text{nd}}^{\text{CN}}$ yield approximately the same results. We note that for decreasing ω_* , the confinement in the x_2 -direction becomes less important. In such a case, the numerical results would indeed be similar to the numerical results of the one-dimensional calculations considered in Section 2.

3.3 Details of the implementation

All simulations of this article are realized in the *Python* programming language using the numerical tools available in *SciPy* [17]. One of the crucial steps is the assembling of the sparse matrices related to the solvers using DTBC. Since these matrices contain small but dense submatrices, one needs to proceed carefully. This task can be realized efficiently by using fast routines to convert dense to sparse matrices followed by a series of sparse `vstack` and `hstack` operations. Another crucial step is the computation of the discrete convolution terms in (62a) and (62b). To this end, we employ parallelized *C*-functions which can be included easily in *Python* programs. All linear systems are solved using direct solvers for sparse matrices which is the most time-consuming part in the stationary as well as in the transient algorithms. We note that no linear system needs to be solved if the time evolution is computed from the explicit Runge-Kutta time-integration method. The timings reported below correspond to an Intel Core i7-4770K CPU @ 3.50GHz \times 8.

4 The Aharonov-Bohm effect

We consider the ring-shaped quantum waveguide depicted in Figure 8, but now we apply an additional homogeneous magnetic field, which is perpendicular to the (x_1, x_2) -plane and which is assumed to vanish outside a circle of radius $r_0 = 10$ nm centered at $(L_1/2, L_2/2)$. For a charged particle in an electromagnetic field, the Hamiltonian of the Schrödinger equation reads

$$\hat{H} = \frac{1}{2m^*}(\hat{p} - qA)^2 + q\Phi, \quad \hat{p} = -i\hbar\nabla, \quad (63)$$

where q is the particle charge and A, Φ denote the vector and scalar potential, respectively. The electric and magnetic fields are expressed in terms of A and Φ via $E = -\partial_t A - \nabla\Phi$

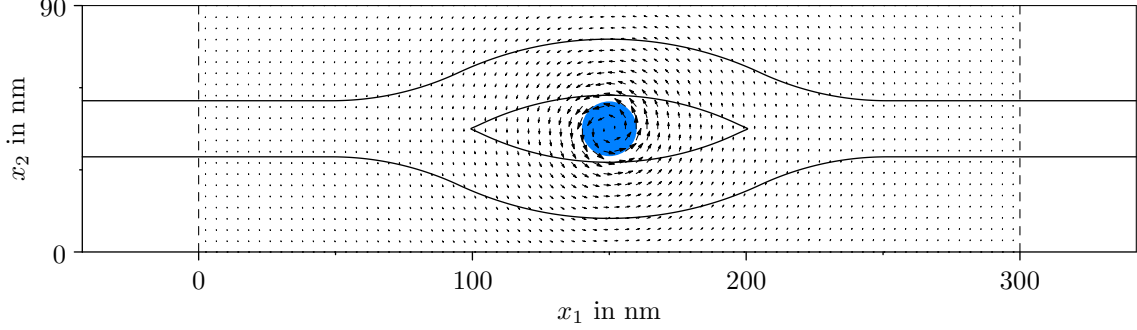


Figure 15: Vector potential (arrows) and magnetic field (blue disk) in the ring-shaped quantum waveguide device depicted in Figure 8. The black solid line indicates an isoline of the potential energy at 200 meV.

and $B = \nabla \times A$. In the simulations below, the vector potential is defined by

$$A(x_1, x_2, x_3) := B_0 \tilde{A}(x_1 - L_1/2, x_2 - L_2/2, x_3), \quad (64)$$

with

$$\tilde{A}(x_1, x_2, x_3) = \begin{cases} \frac{1}{2}(-x_2, x_1, 0)^\top, & \text{if } \sqrt{x_1^2 + x_2^2} \leq r_0, \\ \frac{1}{2}r_0^2(x_1^2 + x_2^2)^{-1}(-x_2, x_1, 0)^\top, & \text{if } \sqrt{x_1^2 + x_2^2} > r_0. \end{cases}$$

Accordingly, the magnetic field reads as

$$B = \begin{cases} (0, 0, B_0)^\top, & \text{if } \sqrt{(x_1 - L_1/2)^2 + (x_2 - L_2/2)^2} \leq r_0, \\ (0, 0, 0)^\top, & \text{if } \sqrt{(x_1 - L_1/2)^2 + (x_2 - L_2/2)^2} > r_0. \end{cases}$$

An illustration of \tilde{A} and B is given in Figure 15. The scalar potential Φ is defined via $V = -e\Phi$.

In order to fix A and Φ , we impose the Coulomb gauge condition $\nabla \cdot A = 0$. Then, using the electron charge $q = -e$, the Hamiltonian in (63) becomes

$$\hat{H} = -\frac{\hbar^2}{2m^*}\Delta - i\frac{e\hbar}{m^*}A \cdot \nabla + \frac{e^2}{2m^*}A^2 + V. \quad (65)$$

Thus, to include the magnetic field into the numerical methods developed in Section 3, we need to discretize two additional terms. The boundary conditions remain unchanged provided that the vector potential vanishes in the exterior domains. In the numerical simulations, we set $A(x_1, x_2, x_3) = 0$ for $x_1 < \delta$ and $x_1 > L_1 - \delta$ ($\delta \approx 2.5$ nm) which is not consistent with (64). However, the development of DTBC in the presence of the vector potential in (64), if at all possible, would be a challenging task. Here, we simply choose L_1 such that $|A(x_1, x_2, x_3)|$ becomes small for $x_1 < \delta$ and $x_1 > L_1 - \delta$. As a result, the modelling error becomes small too, which can be verified by further increasing L_1 . The term $e^2 A^2 / (2m^*)$ in (65) is discretized in the same way as the potential energy. Using the

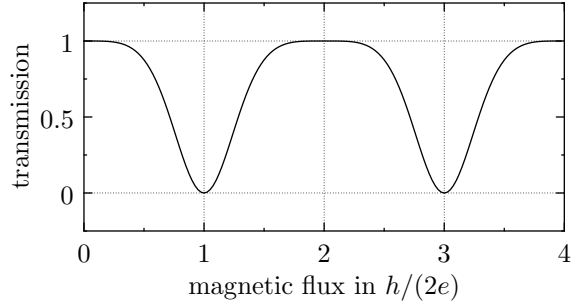


Figure 16: Transmission probability as a function of the magnetic flux in multiples of the flux quantum. The energy of the incoming electrons is fixed at $E_{\text{kin}}^{\text{inc}} = 21.5 \text{ meV}$.

notations corresponding to the case of DTBC described in Section 3, the convection term $-(ie\hbar/m^*)A \cdot \nabla$ is discretized as follows:

$$A \cdot \nabla \approx \text{diag}(A_1)D_{x_1}^1 \otimes I_{J_2} + \text{diag}(A_2)I_{J_1} \otimes D_{x_2}^1.$$

Here, $D_{x_1}^1$, $D_{x_2}^1$ are defined according to (13) and A_1 , A_2 denote the first and second component of the vector potential A , respectively, i.e., $(A_{1,2})_j = (A_{1,2})_{j_1, j_2}$, where $j = j_1 J_2 + j_2$, $j_1 = 0, \dots, J_1$, and $j_2 = 0, \dots, J_2$. The new terms can be easily included into the stationary and transient methods outlined in Section 3.

Let us consider the stationary case first. In particular, we are interested in the transmission probability (55) as a function of the magnetic flux $\Phi_B = B_0 \pi r_0^2$ (not to be confused with the scalar potential Φ). To this end, we compute scattering state solutions of the stationary Schrödinger equation using the Hamiltonian (65). Like in Section 3 we consider electrons injected at the left terminal traveling to the right. While the magnetic flux is increased in each calculation, we keep the kinetic energy of the incoming electrons fixed at $E_{\text{kin}}^{\text{inc}} = 21.5 \text{ meV}$.

Figure 16 shows the computed transmission probability as a function of the magnetic flux in multiples of the flux quantum $\Phi_0 = h/(2e)$. The transmission probability oscillates almost perfectly with increasing values of the magnetic flux. These oscillations are a manifestation of the well-known Aharonov-Bohm effect [1]. In fact, quantum mechanics implies that electrons traveling along a path P , along which $\nabla \times A = 0$, accumulate a phase shift $\varphi = -(e/\hbar) \int_P A \cdot dx$. Hence, using Stokes' theorem, the phase difference between the beam of electrons taking the upper path P_1 and the beam taking the lower path P_2 (see Figure 15) is given by

$$\varphi_1 - \varphi_2 = -\frac{e}{\hbar} \left(\int_{P_1} A \cdot dx - \int_{P_2} A \cdot dx \right) = -\frac{e}{\hbar} \Phi_B.$$

Therefore, the interference of the two electron beams depends solely on the enclosed magnetic flux. The remarkable fact is that the electrons are affected by the vector potential even in regions where the magnetic field is zero which is in strong contrast to classical mechanics.

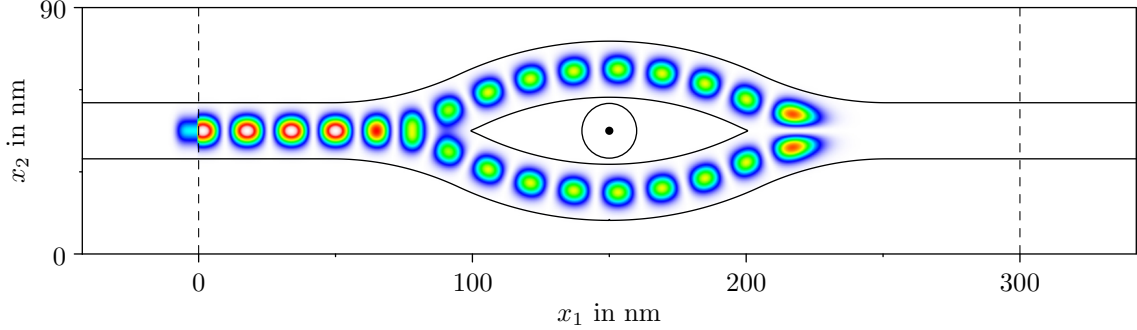


Figure 17: Scattering state solution in a ring-shaped quantum device using the same colormap as in Figure 12. The kinetic energy of the electrons injected at the left contact is $E_{\text{kin}}^{\text{inc}} = 21.5$ meV and the magnetic flux through the encircled area is given by $\Phi_B = h/(2e)$. The black solid line indicates an isoline of the potential energy at 200 meV.

As an example, Figure 17 shows the scattering state solution for $\Phi_B = h/(2e)$ corresponding to the destructive interference condition $|\varphi_1 - \varphi_2| = \pi$. For the calculations, we employed second-order spatial discretizations with $\Delta x = 0.5$ nm corresponding to linear systems of size $N_{\text{DTBC}} = 66\,264$ and $N_{\text{PML}} = 79\,694$. The relative difference between the solutions computed using DTBC and PML is approximately 2×10^{-3} . We note that this value is almost independent from the magnetic flux.

We finally turn our attention to the Aharonov-Bohm effect in the transient regime. In particular, we consider a transient scattering state experiment with the time-dependent vector potential (64). More precisely, we let B_0 change in time as illustrated in Figure 18 (left). Like in the stationary case, we keep the kinetic energy of the incoming electrons fixed at $E_{\text{kin}}^{\text{inc}} = 21.5$ meV. Initially, the magnetic field is switched off and thus the initial wave function corresponds to the scattering state shown in Figure 12. The time evolution of the wave function is illustrated in Figure 19. Figure 18 (right) presents the transmission probability as a function of time.

Between $t = 2$ ps and $t = 2.25$ ps, the magnetic field is increased to a value of $B_0 = \Phi_0/(\pi r_0^2)$, which corresponds to the destructive interference condition considered in the

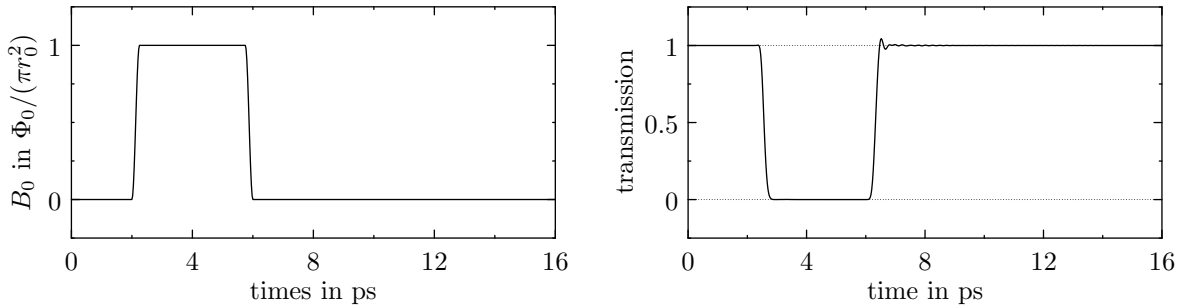


Figure 18: Magnetic field (left) and transmission probability (right) as a function of time.

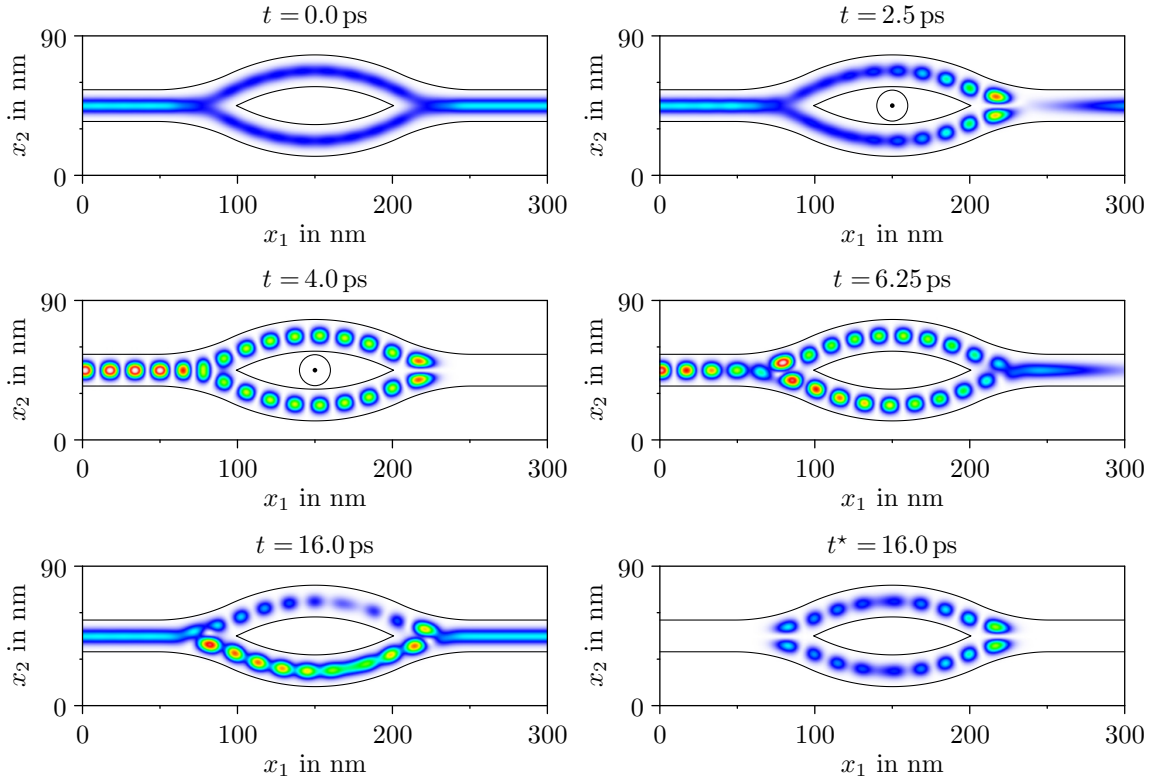


Figure 19: Time evolution of the wave function (probability density) in a transient scattering state experiment with time-dependent magnetic field. The colormap is the same as in Figure 12.

stationary case. The effect on the wave function becomes apparent with a short delay (Fig. 19, $t = 2.5$ ps) and, as expected, the transmission probability decreases. Another 1.5 ps later, the wave function has effectively adopted the scattering state corresponding to the destructive interference condition (Fig. 19, $t = 4$ ps). During the period from $t = 6$ ps to $t = 6.25$ ps, the magnetic field is turned off. Again the wave function starts to evolve in a rather wild manner (Fig. 19, $t = 6.25$ ps). Only a short time later, the transmission probability recovers its old value. However, the wave function does not return to its initial state. Instead we observe strong oscillations restricted to the interior part of the waveguide. Even after another 9.75 ps, these oscillations are still present (Fig. 19, $t = 16$ ps) and in fact they will persist for all time.

This can be demonstrated by decreasing the amplitude of the incoming wave after the second switching operation (which is realized easily in case of PML). A short time later, we are left with an oscillating wave packet which is bound to the region of the ring. The result of such a numerical simulation is depicted in Figure 19 ($t^* = 16$ ps). In this particular example, the amplitude of the incoming wave was multiplied by a factor of 0.999 before each time step with $t \geq 12$ ps. The remaining wave packet is supposed to be a superposition of several eigenstate solutions to the stationary Schrödinger equation.

We note that the probability density of a superposition of several eigenstates is time-dependent. Two eigenstates corresponding to the eigenvalues $E \approx 33.2 \text{ meV}$ and $E \approx 52.8 \text{ meV}$ are shown in Figure 20 but in fact, there are many more eigenstates. The oscillations superimposed to the final wave function are caused by the fast variation of the magnetic field. When B_0 is varied quasi-adiabatically (on the time-scale of about 10 ps), no bound states are excited and hence no oscillations emerge.

The simulation was carried out using the second-order Crank-Nicolson scheme. Alternatively we used the Runge-Kutta time-integration method in combination with a sixth-order spatial discretization and PML. In case of the Crank-Nicolson scheme, we employed a spatial resolution of $\Delta x = 1 \text{ nm}$ and a time-step size of $\Delta t = 0.5 \text{ fs}$. Compared to the simulations presented in the previous sections, this discretization appears to be rather coarse but it should be noted that in the example presented above, we have to solve 32 000 linear systems of size $N_{\text{DTBC}} = 16\,536$ and $N_{\text{PML}} = 20\,046$. If the time evolution is computed using the classical Runge-Kutta method, no linear systems needs to be solved at all (except for the initial scattering state). However, the resulting numerical method is only conditionally stable and hence we cannot use the same time step size as for the Crank-Nicolson method. At a spatial resolution of $\Delta x = 1 \text{ nm}$, we are forced to use a time step size not larger than $\Delta t = 0.25 \text{ fs}$ which agrees well with the condition $\kappa = 9m^*/(16\sqrt{2}\hbar)$ discussed in Section 2.2.

Comparing the simulations on a reduced mesh (see Section 3) with the simulations using the full grid, we found that the results are practically the same. Hence, we did not change the underlying physics by imposing artificial Dirichlet boundary conditions at a distance too close to the center of the waveguides. Eliminating all finite-difference equations corresponding to grid points where the wave function is effectively zero, reduces the size of the linear systems by more than 40 percent and, as a consequence, the time needed to solve the linear systems decreases by more than 50 percent.

The relative difference between the numerical solutions obtained by $\text{DTBC}_{2\text{nd}}^{\text{CN}}$ and $\text{PML}_{2\text{nd}}^{\text{CN}}$ is shown in Figure 21 (left). Compared to the relative differences seen in the simulations of the previous sections, the difference of both numerical solutions is relatively large. This is due to the coarse spatial resolution of $\Delta x = 1 \text{ nm}$ which is twice as large as the resolution employed before. Indeed, a spatial resolution of $\Delta x = 0.5 \text{ nm}$ yields the same level of accuracy as in the previous sections but the simulation becomes extremely time-consuming.

Finally, we report the computing times corresponding to the above mentioned methods in Figure 21 (right). Initially, $\text{DTBC}_{2\text{nd}}^{\text{CN}}$ performs slightly better than $\text{PML}_{2\text{nd}}^{\text{CN}}$. However, the computing time of $\text{DTBC}_{2\text{nd}}^{\text{CN}}$ scales quadratically with the number of time steps and thus, simulations involving even more time steps become very expensive. We note that this problem could be overcome using approximations of the DTBC which can be evaluated more quickly; see, e.g., [6]. As expected, the computing times of the solvers using PML increase linearly. Interestingly, $\text{PML}_{6\text{th}}^{\text{RK4}}$ performs significantly faster than the other methods. Moreover, it is the most accurate method and its implementation is relatively simple.

A movie showing the temporal evolution of the wave function corresponding to the last

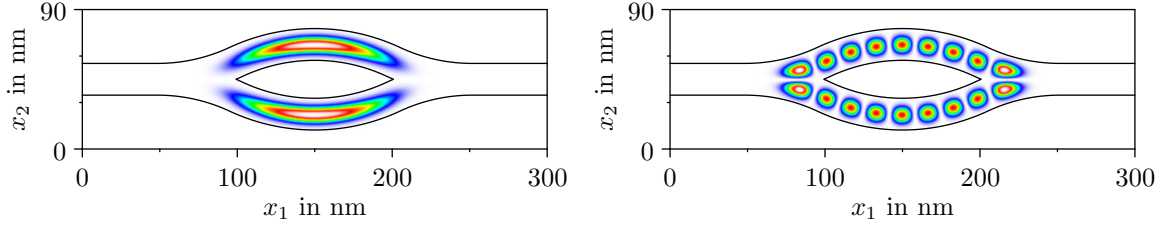


Figure 20: Eigenfunctions to the stationary Schrödinger equation corresponding to the eigenvalues $E \approx 33.2$ meV and $E \approx 52.8$ meV. The probability densities are scaled by their maximum values.

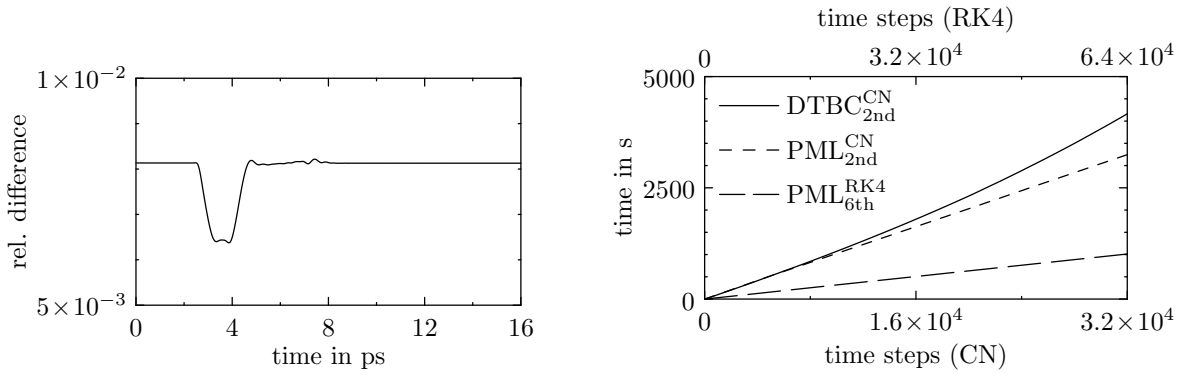


Figure 21: *Left:* Relative difference between the numerical solutions of $\text{DTBC}_{2\text{nd}}^{\text{CN}}$ and $\text{PLM}_{2\text{nd}}^{\text{CN}}$ as a function of time. *Right:* Computing times as a function of the number of time steps.

numerical experiment is available at <http://www.asc.tuwien.ac.at/~juengel>.

Acknowledgements

The authors acknowledge partial support from the Austrian Science Fund (FWF), grants P20214, P22108, I395, and W1245.

References

- [1] Y. Aharonov and D. Bohm. Significance of electromagnetic potentials in the quantum theory. *Phys. Rev.* 115 (1959), 485–491
- [2] X. Antoine, A. Arnold, C. Besse, M. Ehrhardt, and A. Schädle. A review of transparent and artificial boundary conditions techniques for linear and nonlinear Schrödinger equations. *Commun. Comput. Phys.* 4 (2008), 729–796

- [3] X. Antoine and C. Besse. Unconditionally stable discretization schemes of non-reflecting boundary conditions for the one-dimensional Schrödinger equation. *J. Comput. Phys.* 188 (2003), 157–175
- [4] A. Arnold. Numerically absorbing boundary conditions for quantum evolution equations. *VLSI Design* 6 (1998), 313–319
- [5] A. Arnold. Mathematical concepts of open quantum boundary conditions. *Trans. Theory Stat. Phys.* 30 (2001), 561–584
- [6] A. Arnold, M. Ehrhardt, and I. Sofronov. Discrete transparent boundary conditions for the Schrödinger equation: Fast calculation, approximation, and stability. *Commun. Math. Sci.* 1 (2003), 501–556
- [7] A. Arnold and M. Schulte. Transparent boundary conditions for quantum-waveguide simulations. *Math. Computers Simul.* 79 (2008), 898–905
- [8] J.-P. Bérenger. A perfectly matched layer for the absorption of electromagnetic waves. *J. Comput. Phys.* 114 (1994), 185–200
- [9] R. M. Caplan and R. Carretero-González. Numerical stability of explicit Runge-Kutta finite-difference schemes for the nonlinear Schrödinger equation. *Appl. Numer. Math.* 71 (2013), 24–40
- [10] C. Cheng, J.-H. Lee, K. H. Lim, Kim Hwa, H. Z. Massoud, and Q. H. Liu. 3D quantum transport solver based on the perfectly matched layer and spectral element methods for the simulation of semiconductor nanodevices. *J. Comput. Phys.* 227 (2007), 455–471
- [11] W. Chew and W. Weedon. A 3D perfectly matched medium from modified Maxwell’s equations with stretched coordinates. *Microwave Optical Tech. Lett.* 7 (1994), 599–604
- [12] F. Collino. Perfectly matched absorbing layers for the paraxial equations. *J. Comput. Phys.* 131 (1997), 164–180
- [13] J. Davies. *The Physics of Low-dimensional Semiconductors: An Introduction* (Cambridge University Press, 1998)
- [14] B. Ducomet, A. Zlotnik, and A. Romanova. A splitting higher order scheme with discrete transparent boundary conditions for the Schrödinger equation in a semi-infinite parallelepiped. Preprint, 2013. [arXiv:1309.7280](https://arxiv.org/abs/1309.7280)
- [15] J.-P. Gazeau. *Coherent states in quantum physics* (Wiley, 2009)
- [16] E. K. Heller and F. C. Jain. Simulation of one-dimensional ring quantum interference transistors using the time-dependent finite-difference beam propagation method. *J. Appl. Phys.* 87 (2000), 8080–8087

- [17] E. Jones, T. Oliphant, P. Peterson, and others. SciPy: Open source scientific tools for Python (2001–). <http://www.scipy.org/>
- [18] C. Lent and D. Kirkner. The quantum transmitting boundary method. *J. Appl. Phys.* 67 (1990), 6353–6359
- [19] C. Lubich and A. Schädle. Fast convolution for non-reflecting boundary conditions. *SIAM J. Sci. Comput.* 24 (2002), 161–182
- [20] W. W. Lui and M. Fukuma. Exact solution of the Schrödinger equation across an arbitrary one-dimensional piecewise-linear potential barrier. *J. Appl. Phys.* 60 (1986), 1555–1559
- [21] J.-F. Mennemann, A. Jüngel, and H. Kosina. Transient Schrödinger-Poisson Simulations of a high-frequency resonant tunnelling diode oscillator. *J. Comput. Phys.* 239 (2013), 187–205
- [22] F. Schmidt and P. Deuffhard. Discrete transparent boundary conditions for the numerical solution of Fresnel's equation. *Comput. Math. Appl.* 29 (1995), 53–76
- [23] M. Schulte and A. Arnold. Discrete transparent boundary conditions for the Schrödinger equation – a compact higher order scheme. *Kinetic Related Models* 1 (2008), 101–125
- [24] I. Singer and E. Turkel. A perfectly matched layer for the Helmholtz equation in a semi-infinite strip. *J. Comput. Phys.* 201 (2004) 439–465
- [25] B. Szafran and F. Peeters. Time-dependent simulations of electron transport through a quantum ring: Effect of the Lorentz force. *Phys. Rev. B* 72 (2005), 165301 (8 pages)
- [26] E. Turkel and A. Yefet, Absorbing PML boundary layers for wave-like equations. *Appl. Numer. Math.* 27 (1998), 533–557
- [27] S. Vatannia and G. Gildenblat. Airy's functions implementation of the transfer-matrix method for resonant tunneling in variably spaced finite superlattices. *IEEE J. Quantum Electron.* 32 (1996), 1093–1105
- [28] C. Zheng. A perfectly matched layer approach to the nonlinear Schrödinger wave equations. *J. Comput. Phys.* 227 (2007), 537–556
- [29] S. Zhou and X. Cheng. Numerical solution to coupled nonlinear Schrödinger equations in unbounded domains. *Math. Computers Simul.* 80 (2010), 2362–2373
- [30] A. Zlotnik and I. Zlotnik. Finite element method with discrete transparent boundary conditions for the time-dependent 1D Schrödinger equation. *Kinetic Related Models* 5 (2012), 639–667